RMetS
Royal Meteorological Society

Moisture statistics in free convective boundary layers growing into linearly stratified atmospheres

Juan Pedro Mellado,[a]* Marc Puche[a] and Chiel C. van Heerwaarden[b]
[a]*Max Planck Institute for Meteorology, Hamburg, Germany*
[b]*Meteorology and Air Quality Group, Wageningen University, The Netherlands*

*Correspondence to: J. P. Mellado, Max Planck Institute for Meteorology, Bundesstrasse 53, 20146 Hamburg, Germany. E-mail: juan-pedro.mellado@mpimet.mpg.de

We use dimensional analysis and direct numerical simulations to characterize specific humidity statistics in the equilibrium (quasi-steady) entrainment regime of cloud-free convective boundary layers that grow into linearly stratified free atmospheres. The first three moments and the mean vertical flux are studied for arbitrary combinations of free-atmosphere lapse-rates and surface fluxes of buoyancy and specific humidity. First, we find the combination of these parameters that distinguishes between the entrainment-drying regime and the surface-moistening regime. We also provide a zero-order model describing both regimes. Second, we parametrize the variances in the mixed layer and in the entrainment zone separately, based on convective and entrainment-zone scales, respectively. We show that the large variances in the entrainment zone are not only due to large production rates, but also due to low dissipation rates. Third, we provide the skewness for any regime between the pure drying limit and the pure moistening limit. The variation of the skewness indicates that knowing the sign of the skewness near the surface is often insufficient to distinguish between drying and moistening regimes, in contrast to previous conjectures. In a more general context, this paper further supports the applicability of direct numerical simulations to investigate the atmospheric boundary layer, as inferred from the degree of Reynolds number similarity observed in the results and from the consistency of the derived parametrizations with field measurements.

Key Words: moisture; free convection; top-down–bottom-up decomposition; direct numerical simulation

Received 18 March 2017; Revised 7 June 2017; Accepted 8 June 2017; Published online in Wiley Online Library 27 July 2017

1. Introduction

Surface processes and cloud formation critically depend on the moisture field in the planetary boundary layer. Measurement campaigns and numerical simulations have provided considerable insights into moisture properties during the last decades. For instance, we have learned to distinguish between drying and moistening regimes depending on the ratio between entrainment and surface fluxes, we have learned that the variance of the specific humidity peaks in the entrainment zone, and we have also learned that dry air from the free atmosphere can penetrate deep into the boundary layer, which favours a negative skewness of the specific humidity in most of the mixed layer (e.g. Deardorff, 1974; Mahrt, 1991; Couvreux *et al.*, 2007; Turner *et al.*, 2014; Wulfmeyer *et al.*, 2016, and references therein).

However, that previous work is mainly based on single-case studies, i.e. particular combinations of surface fluxes and free-atmosphere lapse-rates, and we are still missing the parametrizations that allow us to extrapolate those results, quantitatively, to different meteorological conditions. This paper provides these parametrizations for one regime of the planetary boundary layer, namely, the equilibrium (quasi-steady) entrainment regime of a free convective boundary layer (CBL) that grows into a linearly stratified atmosphere (Fedorovich *et al.*, 2004). This regime occurs over land in strongly convective conditions, e.g. during the late morning and early afternoon period. In particular, we systematically analyze the specific humidity field, and we parametrize its first three moments and mean vertical flux for arbitrary meteorological conditions, which in that regime means for arbitrary combinations of surface fluxes and free-atmosphere lapse-rates of buoyancy and specific humidity.

We first study the transition between drying and moistening regimes. For typical atmospheric conditions, entrainment tends to dry the CBL whereas evapotranspiration tends to moisten it. These

two counteracting processes are characterized by the entrainment moisture flux and the surface moisture flux. When the former dominates, the CBL is in the entrainment-drying regime; when the latter dominates, the CBL is the surface-moistening regime. This understanding has been well documented using observational and numerical data (e.g. Mahrt, 1991; Couvreux *et al.*, 2007). However, in the equilibrium (quasi-steady) entrainment regime of a CBL, the entrainment flux is *a priori* unknown. This motivates the first goal of this paper: to find a parametrization of the entrainment flux to predict the meteorological conditions for the transition between drying and moistening regimes.

The second goal of this paper is to characterize the specific humidity variance. Understanding and parametrizing the moisture variance is crucial for accurately representing cloud formation in atmospheric models (e.g. Lewellen and Yoh, 1993; Neggers *et al.*, 2006; Siebert and Shaw 2017, and references therein). Previous work has shown that, for typical atmospheric conditions, the moisture variance peaks in the entrainment zone (Moeng and Wyngaard, 1984; Mahrt, 1991) and is not characterized by the convective scales that characterize the variance in the mixed layer (Deardorff, 1974; Sorbjan, 2005). In general and not only for the moisture, parametrizing entrainment-zone properties as a function of the meteorological conditions has remained challenging for decades, partly due to the lack of accurate data. Recently, Garcia and Mellado (2014) provided parametrizations for buoyancy properties in the entrainment zone of a shear-free CBL using data from direct numerical simulation (DNS). Here, we extend this work and provide parametrizations for the specific humidity.

Last, we investigate the skewness. The moisture skewness is equally important for cloud formation, since condensation can only occur once the positive tail of the probability density function of specific humidity surpasses the saturation vapour humidity (e.g. Lewellen and Yoh, 1993; Naumann *et al.*, 2013). Qualitatively, we know that the specific humidity skewness is predominantly negative in most of the mixed layer and becomes positive in the upper part of the entrainment zone (Deardorff, 1974; Mahrt, 1991). We also know that the behaviour in the lower part of the CBL is more variable, becoming positive when surface moistening is strong enough (Mahrt, 1991; Couvreux *et al.*, 2007). However, a complete characterization of the moisture skewness for arbitrary meteorological conditions is still missing. We provide it here for a shear-free CBL penetrating into a linearly stratified atmosphere as a function of the surface fluxes and free-atmosphere lapse-rates. Our analysis also shows that knowing the sign of the skewness is often insufficient to distinguish between drying and moistening regimes, in contrast to previous conjectures based on single-case studies (Mahrt, 1991; Couvreux *et al.*, 2007).

The analysis presented in this paper is based on DNS, dimensional analysis, and a top-down–bottom-up decomposition of the specific humidity. This formulation allows us to investigate

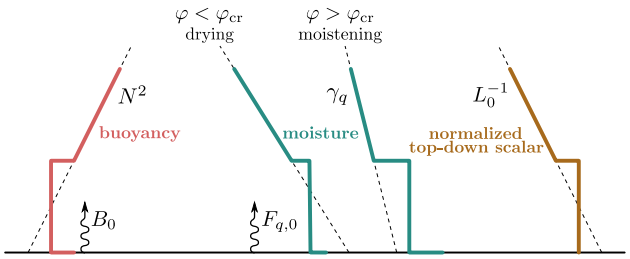

Figure 1. Sketch of the vertical profiles of buoyancy, b, specific humidity, q, and normalized top-down scalar, χ. The parameters defining the problem are the kinematic surface fluxes B_0 and $F_{q,0}$, and the lapse rates in the free atmosphere $-N^2$ and γ_q. The flux-ratio parameter, φ, is defined in Eq. (38). The sketch depicts two different moisture regimes: entrainment-drying regime ($\varphi < \varphi_{cr}$) and surface-moistening regime ($\varphi > \varphi_{cr}$). [Colour figure can be viewed at wileyonlinelibrary.com].

the aforementioned dependencies on the surface fluxes and free-atmosphere lapse-rates with one single simulation, and all that remains is to ascertain the sensitivity of the results to the Reynolds number. After explaining this formulation in section 2, results are presented in two sections before the conclusions: section 3 discusses statistical properties of the top-down scalar, and section 4 constructs and discusses statistical properties of the specific humidity.

2. Formulation

We consider a convective boundary layer that grows into a linearly stratified atmosphere without clouds and without a mean wind (Figures 1 and 2). The background profiles of buoyancy and specific humidity in the free atmosphere are, respectively,

$$b_{bg} \equiv N^2 z\,, \tag{1a}$$

$$q_{bg} \equiv q_{bg,0} - \gamma_q z\,, \tag{1b}$$

where $-N^2$ and γ_q are the lapse rates, and z is the vertical distance from the surface. The subscript 'bg' indicates background. A list of symbols is presented in Table 1. The surface is aerodynamically smooth, and the surface kinematic fluxes of buoyancy and specific humidity, B_0 and $F_{q,0}$, are constant and horizontally homogeneous. We assume $F_{q,0} \geq 0$ and $\gamma_q \geq 0$, i.e. a moist surface and a dry free atmosphere.

2.1. *Governing equations*

We consider the Navier–Stokes equations under the Boussinesq approximation (Panton, 2005; Wyngaard, 2010):

$$\partial_t u_i + u_j \partial_j u_i = -\partial_i p + \nu \partial_{jj} u_i + b\delta_{i3}\,, \tag{2a}$$

$$\partial_j u_j = 0\,, \tag{2b}$$

$$\partial_t b + u_j \partial_j b = \kappa \partial_{jj} b\,, \tag{2c}$$

$$\partial_t q + u_j \partial_j q = \kappa \partial_{jj} q\,. \tag{2d}$$

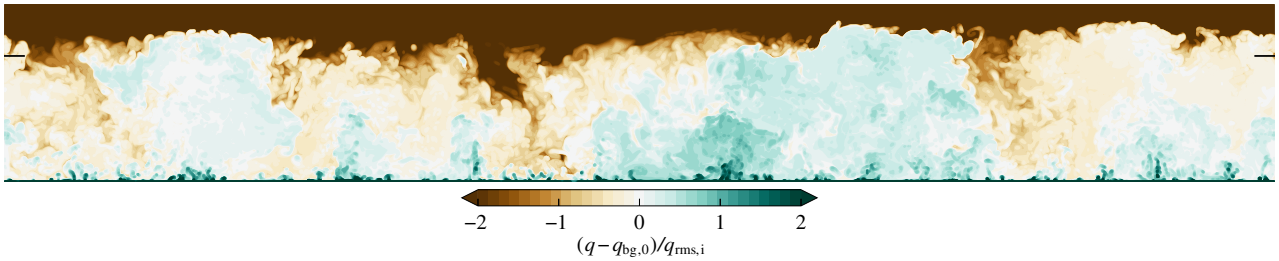

Figure 2. Vertical cross-section of the specific humidity for $\varphi = \varphi_{cr}$, i.e. at the transition between drying and moistening regimes. The field is normalized with the humidity rms in the entrainment zone, $q_{rms,i}$ (Eq. (65)). The short horizontal lines at both sides of the figure indicate $z = z_{enc}$, i.e., the CBL depth defined in terms of the encroachment length-scale (Eq. (5)). Data correspond to case $Re_0 = 117$ at $z_{enc}/L_0 = 21.5$ (cf. Table 2). [Colour figure can be viewed at wileyonlinelibrary.com].

Table 1. List of most relevant symbols. The symbol ξ can be the buoyancy b, the moisture q, or the normalized top-down scalar χ.

Symbol	Description
F_ξ	Mean vertical flux of ξ. The symbol B is used for the buoyancy flux, following previous literature.
$F_{\xi,\mathrm{i}}$	Entrainment flux, defined as the local maximum of the magnitude of F_ξ near the CBL top when this maximum exists.
$F_{\xi,1}$	Reference entrainment flux (e.g. Eq. (41) for q).
$F_{\xi,0}$	Surface flux, a constant in this study.
$F_{\xi,\mathrm{ref}}$	Reference flux, sum of surface flux and reference entrainment flux.
L_0	Reference Ozmidov scale, defined by Eq. (4).
Re_0	Reference Reynolds number, defined by Eq. (3).
z_{enc}	Encroachment length-scale, defined by Eq. (5).
$z_{\mathrm{i,f}\xi}$	Height of the local maximum of the magnitude of F_ξ near the CBL top.
$z_{\mathrm{i,g}\xi}$	Height of the local maximum of the magnitude of the mean gradient near the CBL top.
γ_ξ	Lapse rate in the free atmosphere, a constant in this study. It is equal to $-N^2$ for the buoyancy.
δ_ξ	Gradient thickness of the transition layer between the entrainment zone and the free atmosphere (e.g. Eq. (B2) for q).
ξ_{bg}	Background profile in the free atmosphere.
ξ_{enc}	Encroachment scale of ξ.
ξ_{ml}	Vertically averaged value between between 0 and z_{enc} (e.g. Eq. (48) for q).
ξ_{ref}	Reference scale of ξ (e.g. Eq. (39a) for q).
$\xi_{\mathrm{rms,i}}$	Local maximum of the root-mean-square of ξ near the CBL top.
φ	Moisture flux-ratio parameter, defined by Eq. (38).

The variable u_i is the velocity component in the direction of the unit vector $\mathbf{e}_i$, p is a modified pressure divided by the constant reference density, b is the buoyancy, and q is the specific humidity. The parameter ν is the kinematic viscosity, and κ is the thermal diffusivity. Equation (2c) can be derived from the evolution equations of the energy variable (e.g. potential temperature or static energy) and specific humidity assuming that the mass diffusivity of water vapour is equal to the thermal diffusivity, once b has been expressed as a linear combination of the energy variable and specific humidity by linearizing the equations of state. The operators ∂_t and ∂_j are the partial derivatives with respect to time, t, and with respect to the spatial coordinate x_j, and δ_{ij} is the Kronecker delta. The Einstein summation convention applies to Roman-letter indices throughout.

No-penetration, no-slip boundary conditions are imposed at the bottom boundary of the computational domain, and no-penetration, free-slip boundary conditions are imposed at the top boundary. For the buoyancy and specific humidity, we use the Neumann boundary conditions $\partial_z b = N^2$ and $\partial_z q = -\gamma_q$ at the top boundary, and $\partial_z b = -B_0/\kappa$ and $\partial_z q = -F_{q,0}/\kappa$ at the bottom boundary (i.e. constant kinematic fluxes at the top and at the bottom). Periodicity applies at the lateral boundaries.

We use DNS, i.e. we solve the Navier–Stokes equations directly, without any turbulence model (Coleman *et al.*, 1990; Moin and Mahesh, 1998). This technique removes the uncertainty associated with turbulence models and numerical artifacts, which proves convenient in the near-surface region and in the entrainment zone because small scales become relevant there (Figure 2). Despite Reynolds numbers in DNS being small compared to those in the atmosphere, DNS is reaching a degree of Reynolds number similarity that allows certain extrapolation of the results to atmospheric conditions (e.g. Mellado, 2012; Jonker *et al.*, 2013; Waggy *et al.*, 2013; Garcia and Mellado, 2014; van Heerwaarden and Mellado, 2016).

Equations (2) are solved on a collocated, structured grid using sixth-order, spectral-like compact finite differences to approximate spatial derivatives (Lele, 1992), and using a low-storage, fourth-order Runge–Kutta scheme to advance the discretized equations in time (Carpenter and Kennedy, 1994). The divergence-free (or solenoidal) constraint is imposed by decomposing the pressure-Poisson equation inside the periodic, horizontal planes using a Fourier transform (Frigo and Johnson, 2005), and by factorizing the resulting set of equations along the vertical direction (Mellado and Ansorge, 2012). Source files with the implementation of this numerical algorithm and further documentation can be found at https://github.com/turbulencia/tlab (accessed 28 June 2017).

2.2. *Dimensional analysis*

Dimensional analysis allows us to minimize the number of simulations needed in the study (e.g. Panton, 2005). We apply it in this section to the CBL dynamics, and in section 4 to the specific humidity. From Eqs (2a)–(2c) and the corresponding boundary conditions, we can infer that the control parameters $\{\nu, \kappa, B_0, N\}$ fully characterize the CBL dynamics after an initial transient or spin-up period, once the initial conditions have been sufficiently forgotten. This set reduces to two non-dimensional parameters, viz. the Prandtl number ν/κ and a reference Reynolds number

$$Re_0 \equiv B_0/(N^2\nu)\ . \tag{3}$$

Hence, without loss of generality, one single simulation allows us to study the system for arbitrary combinations of surface buoyancy flux, B_0, and stratification strength of the free atmosphere, N^2, for a given Prandtl number and Reynolds number (also Garcia and Mellado, 2014; Mellado *et al.*, 2016). We set the Prandtl number equal to 1, which is a good approximation to the atmospheric value ≈ 0.7, and we investigate the sensitivity of the results to Re_0.

We will express the dependence of statistical properties on height and time in terms of the non-dimensional variables z/z_{enc} and z_{enc}/L_0, where L_0 is the reference Ozmidov scale (Garcia and Mellado, 2014)

$$L_0 \equiv (B_0/N^3)^{1/2}, \tag{4}$$

and $z_{\mathrm{enc}}(t)$ is the encroachment length-scale (Garcia and Mellado, 2014; van Heerwaarden and Mellado, 2016)

$$z_{\mathrm{enc}} \equiv \left\{2N^{-2}\int_0^{z_\infty}(\langle b\rangle - b_{\mathrm{bg}})\,\mathrm{d}z\right\}^{1/2}. \tag{5}$$

Henceforth, angle brackets indicate a horizontal average.

The length-scale L_0 is referred to as reference Ozmidov scale because it provides an estimate for the Ozmidov scale $(\varepsilon/N^3)^{1/2}$ in the CBL (Ozmidov, 1965; Smyth and Moum, 2000), since the viscous dissipation rate in the CBL is an order-of-one fraction of B_0. L_0 proves useful in the discussion that follows because it characterizes the upper region of the entrainment zone, where the buoyancy stratification of the free atmosphere directly affects the flow dynamics (Garcia and Mellado, 2014). Typical midday atmospheric values of L_0 vary between 20 and 200 m.

The length-scale z_{enc} characterizes the CBL depth (cf. Figure 2). We refer to it as the encroachment scale because it reduces to the CBL depth in the encroachment regime of mixed-layer models (Lilly, 1968; Carson and Smith, 1975). We use the symbol z_{enc} to distinguish this length from CBL depths defined in terms of local properties in the entrainment zone, like the point of maximum

buoyancy gradient or the point of minimum buoyancy flux, for which the symbol z_i is commonly used in the literature. These pointwise definitions of the CBL depth are commensurate with z_{enc} (Sullivan *et al.*, 1998; Garcia and Mellado, 2014). The encroachment length-scale has the advantage that it is an integral definition, which is more robust than a pointwise definition, and its time dependence can be obtained analytically by integrating the following evolution equation for the mean buoyancy:

$$\partial_t(\langle b\rangle - b_{bg}) = \partial_z(\kappa\partial_z\langle b\rangle - \langle b'w'\rangle)\,. \tag{6}$$

This equation follows from averaging Eq. (2c) and from the assumption that the background buoyancy profile is constant in time (Eq. (1a)). The integration yields

$$z_{enc}/L_0 = \left\{2(1+Re_0^{-1})N(t-t_0)\right\}^{1/2}, \tag{7}$$

t_0 being an integration constant. The ratio z_{enc}/L_0 is a measure of the scale separation between the CBL depth and the depth of the upper region of the entrainment zone. For typical midday atmospheric conditions $z_{enc} \approx 1000-2000$ m, the ratio z_{enc}/L_0 varies between 5 and 50. We focus on the equilibrium (quasi-steady) entrainment regime, which sets in for $z_{enc}/L_0 \gtrsim 10-15$ (Fedorovich *et al.*, 2004; Garcia and Mellado, 2014).

2.3. Definition of the normalized top-down scalar

Our analysis is based on a top-down–bottom-up decomposition of the specific humidity (Moeng and Wyngaard, 1984; Wyngaard and Brost, 1984). We adopt this approach because q becomes a passive scalar when the problem is formulated in terms of b and q instead of temperature and q – changing q without changing b does not alter the CBL dynamics – and passive scalars can be conveniently analyzed with such a decomposition (e.g. Cuijpers and Holtslag, 1998; Patton *et al.*, 2003; de Roode *et al.*, 2004; Moene *et al.*, 2006).

There are two major steps in this approach. First, we define a normalized top-down scalar as a linear combination of q and b according to

$$\chi \equiv \frac{q - q_{bg,0} - (F_{q,0}/B_0)\,b}{\gamma_q L_0 + (F_{q,0}/B_0)N^2 L_0} \tag{8}$$

(cf. Figure 1). The numerator ensures that the surface flux of χ is zero, which is the condition defining a top-down scalar. The denominator normalizes χ such that vertical displacements of order L_0 in the free atmosphere induce scalar variations of order 1; this normalization is not necessary, but it is convenient to simplify the expressions in the following sections. From Eq. (8) and the evolution equations for the buoyancy and specific humidity (Eqs (2c) and (2d)), we obtain the following evolution equation for χ:

$$\partial_t\chi + u_j\partial_j\chi = \kappa\partial_{jj}\chi\,. \tag{9}$$

The boundary conditions are $\partial_z\chi = 0$ at the bottom boundary of the computational domain, and $\partial_z\chi = -L_0^{-1}$ at the top boundary. From Eq. (8) and the definitions of the background profiles of buoyancy and specific humidity (Eqs (1)), we obtain the following background profile for χ:

$$\chi_{bg} = -z/L_0\,. \tag{10}$$

The lapse rate of χ in the free atmosphere is thus L_0^{-1}. We will use these definitions extensively in the following sections.

The second step is to substitute the evolution equation for the specific humidity (Eq. (2d)), by that of the top-down scalar (Eq. (9)). The advantage of this substitution is that one single simulation with b and χ allows us to construct q for any moisture condition $\{F_{q,0},\ \gamma_q,\ q_{bg,0}\}$ according to

$$q = q_{bg,0} + (F_{q,0}/B_0)\,b + \left\{\gamma_q L_0 + (F_{q,0}/B_0)N^2 L_0\right\}\chi, \tag{11}$$

after an initial transient (Appendix A). Since the dependence of b and χ on B_0 and N^2 can be inferred from one single simulation, this relationship implies that one single simulation is sufficient to study the dependence of the specific humidity on the control parameters $\{B_0,\ N^2,\ \gamma_q,\ F_{q,0}\}$ indicated in Figure 1. Additionally, we need to study the sensitivity of the results to the reference Reynolds number Re_0.

2.4. Description of the simulations

We consider three simulations with three different reference Reynolds numbers. Table 2 presents basic parameters. Cases $Re_0 = 42$ and $Re_0 = 117$ have been studied before by Garcia and Mellado (2014) and by Mellado *et al.* (2016) and further details of the simulations can be found there. The final states of development of the CBL in that previous work were $z_{enc}/L_0 = 25.7$ for $Re_0 = 42$ and $z_{enc}/L_0 = 18.0$ for $Re_0 = 117$. For the current analysis, we have added χ at those times and continued the simulations until $z_{enc}/L_0 = 33.0$ and $z_{enc}/L_0 = 21.7$. In the analysis below, we have used data only after $z_{enc}/L_0 = 27.0$ and $z_{enc}/L_0 = 19.0$, respectively, to remove part of the initial transient. Additionally, we have considered a third case with $Re_0 = 25$, to better assess the dependence of the results on the Reynolds number. This third case is defined analogously to the previous two cases, but retains the top-down scalar from the beginning of the simulation, when $z_{enc}/L_0 \approx 0$.

3. Top-down scalar

This section characterizes the mean, the variance, and the skewness of the top-down scalar χ as a function of the variables $\{z/z_{enc},\ z_{enc}/L_0\}$ and the parameter Re_0 (cf. section 2.2). The motivation is twofold. First, the top-down scalar represents the specific humidity in the pure drying regime, i.e. when the moisture surface flux is negligible. Second, this characterization is later used in section 4 to parametrize the corresponding specific humidity statistics as a function of the control parameters $\{B_0,\ N^2,\ \gamma_q,\ F_{q,0}\}$ indicated in Figure 1.

Table 2. Simulation parameters.

Re_0	Grid	Domain size	z_{enc}/L_0	Re_*	Re_t
25	$1280^2 \times 512$	$(215\,L_0)^2 \times 162\,L_0$	35.9	2960	1440
42	$2560^2 \times 896$	$(215\,L_0)^2 \times 81\,L_0$	33.0	4420	2400
117	$5120^2 \times 1024$	$(215\,L_0)^2 \times 64\,L_0$	21.7	7060	4120

Columns 4–6 correspond to the final time in each of the three simulations. The reference Ozmidov scale, L_0, is defined in Eq. (4). The encroachment length scale, z_{enc}, is defined in Eq. (5). The convective Reynolds number is defined as $Re_* \equiv z_{enc}w_*/\nu$, where w_* is the convective velocity (Eq. (30a)). The turbulent Reynolds number is defined as $Re_t \equiv \max_z\{e^2/(\varepsilon\nu)\}$, where $e \equiv \langle u_i'u_i'\rangle/2$ is the turbulence kinetic energy and $\varepsilon \equiv \nu\langle(\partial_k u_i' + \partial_i u_k')\partial_k u_i'\rangle$ is its viscous dissipation rate; a Taylor-scale Reynolds number can be calculated as $\sqrt{(20/3)Re_t}$ (Pope, 2000).

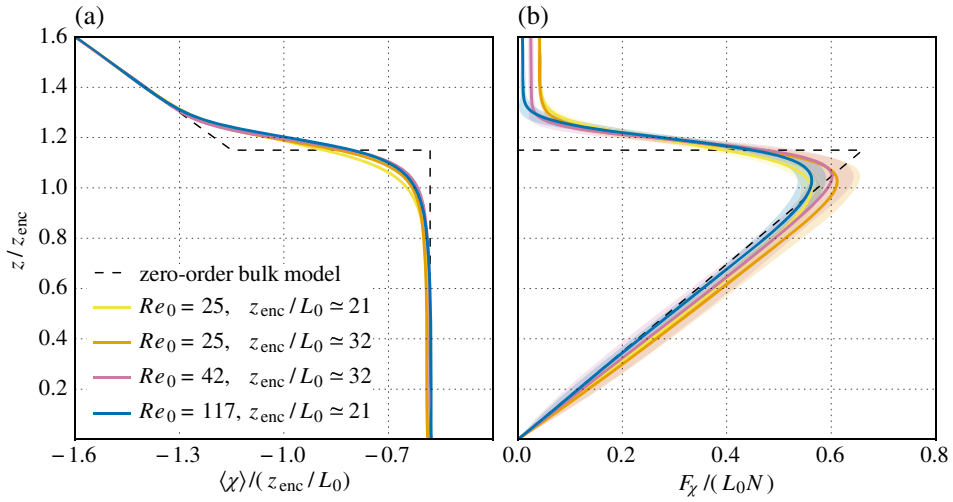

Figure 3. Normalized profiles of (a) the mean top-down scalar and (b) its mean vertical flux. Lines indicate time averages over 3–8 convective time-scales z_{enc}/w_* (5–8% of z_{enc}/L_0), and shadows mark intervals of two standard deviations around those averages. [Colour figure can be viewed at wileyonlinelibrary.com].

3.1. *Mean properties and bulk analysis*

The mean buoyancy profile is characterized by the set of encroachment scales $\{z_{enc}, b_{enc}\}$, where

$$b_{enc} \equiv N^2 z_{enc}\,. \tag{12}$$

This means that the function $b_{enc}^{-1}\langle b\rangle(z/z_{enc}, z_{enc}/L_0)$ is of order one and becomes self-similar as the CBL expands in time (i.e. independent of z_{enc}/L_0 and only a function of the normalized height z/z_{enc}). In particular, the vertically averaged buoyancy

$$b_{ml} \equiv z_{enc}^{-1}\int_0^{z_{enc}} \langle b\rangle\, dz \tag{13}$$

varies as $b_{ml} = \beta\, b_{enc}$, where $\beta = 1.01 \pm 0.01$ (Garcia and Mellado, 2014).

Similarly, we define a vertically averaged scalar by

$$\chi_{ml} \equiv z_{enc}^{-1}\int_0^{z_{enc}} \langle\chi\rangle\, dz, \tag{14}$$

and we use an integral analysis of the evolution equation for χ (Eq. (9)) to find an appropriate characteristic scale, χ_{enc}. This integral analysis yields

$$\int_0^{z_\infty} (\langle\chi\rangle - \chi_{bg})\, dz = -\kappa L_0^{-1}(t - t_{\chi,0}), \tag{15}$$

where $t_{\chi,0}$ is an integration constant equivalent to t_0 in Eq. (7). The left-hand side can be estimated as

$$\begin{aligned}\int_0^{z_\infty} (\langle\chi\rangle - \chi_{bg})\, dz &\approx \int_0^{z_{enc}} (\langle\chi\rangle - \chi_{bg})\, dz \\ &= \chi_{ml} z_{enc} + (1/2) L_0^{-1} z_{enc}^2\,.\end{aligned} \tag{16}$$

The right-hand side of Eq. (15) can be estimated as

$$\kappa L_0^{-1}(t - t_{\chi,0}) \approx \kappa L_0^{-1}(t - t_0) = \frac{L_0^{-1} z_{enc}^2}{2Pr(Re_0 + 1)} \tag{17}$$

when $t \gg t_{\chi,0}$ and $t \gg t_0$, i.e. when the initial conditions have been sufficiently forgotten. The last equality stems from Eq. (7). For the high Reynolds numbers characteristic of the atmosphere, $Re_0 \approx 10^6$–10^7, this term is always negligible compared to any of the two terms in Eq. (16), i.e. the decrease of χ_{ml} by the downward molecular flux is negligible compared to the decrease by turbulent mixing with the free atmosphere. Hence, the integral analysis of the evolution equation for χ yields the estimate $\chi_{ml} \approx -(1/2)\, z_{enc}/L_0$, which suggests the definition

$$\chi_{enc} \equiv -(1/2) L_0^{-1} z_{enc} \tag{18}$$

as encroachment scale for χ. The self-similar behaviour of the normalized profiles in Figure 3(a) confirms z_{enc} and χ_{enc} as characteristic scales for the mean scalar, and we can write $\chi_{ml} = \beta_\chi\, \chi_{enc}$, where $\beta_\chi \approx 1.16$ (Table 3). We observe that values corresponding to different Reynolds numbers are within 2%, indicating a degree of Reynolds number similarity that supports certain extrapolation of the results to atmospheric conditions. This convergence towards Reynolds number similarity is further discussed in section 4.

The mean vertical flux

$$F_\chi \equiv \langle\chi' w'\rangle - \kappa\,\partial_z\langle\chi\rangle \tag{19}$$

can also be partly characterized from the analysis of the evolution equation for $\langle\chi\rangle$; henceforth, primes indicate turbulent-fluctuation fields, e.g. $\chi' = \chi - \langle\chi\rangle$. First, taking the vertical derivative of the two sides of this evolution equation yields that F_χ is approximately linear with respect to z, since the shape of the vertical profile of $\langle\chi\rangle$ is approximately time invariant in the mixed layer (Figure 3(a)). Hence, F_χ increases from 0 at the surface (the boundary condition) to a maximum $F_{\chi,i}$ near the inversion. We will refer to $F_{\chi,i}$ as entrainment flux of the top-down scalar. Second, an order-of-magnitude analysis provides the following estimate of the entrainment flux:

$$F_{\chi,i} \sim -z_{enc}\frac{d\chi_{enc}}{dt} = \frac{1}{2} z_{enc} w_{enc} L_0^{-1} \approx \frac{1}{2} L_0 N, \tag{20}$$

where

$$w_{enc} \equiv \frac{dz_{enc}}{dt} \tag{21}$$

is a mean entrainment velocity. We have used the approximation $z_{enc} w_{enc} \approx L_0^2 N$, valid for high enough Reynolds numbers (cf. Eq. (7)). Figure 3 confirms this analysis: when normalized with z_{enc} and $L_0 N$, profiles of F_χ behave self-similarly and reach a maximum magnitude between 0.55 and 0.60 near the inversion (Table 3).

Table 3. Self-similar constants of mean properties of the top-down scalar.

Re_0	$\chi_{\rm ml}/\chi_{\rm enc}$	$F_{\chi,{\rm i}}/(L_0N)$	$z_{{\rm i,g}\chi}/z_{\rm enc}$	$z_{{\rm i,f}\chi}/z_{\rm enc}$
25	1.18	0.57	1.19	0.98
42	1.16	0.59	1.19	1.01
117	1.16	0.56	1.20	0.99

The mixed-layer value is defined by Eq. (14), and the encroachment scale by Eq. (18). In the last two columns, $z_{{\rm i,g}\chi}$ is the height of minimum mean gradient, and $z_{{\rm i,f}\chi}$ is the height of maximum flux, $F_{\chi,{\rm i}}$.

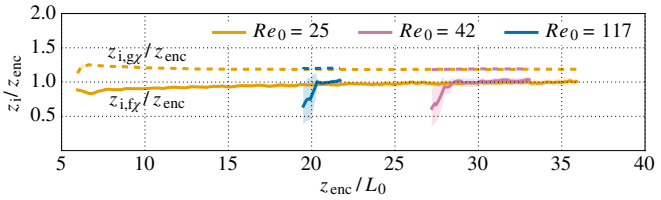

Figure 4. Temporal evolution of the normalized heights of the minimum mean gradient of top-down scalar, $z_{{\rm i,g}\chi}$, and of its maximum mean flux, $z_{{\rm i,f}\chi}$. Lines indicate time averages within an interval $\Delta z_{\rm enc}/L_0 = 1$, and shadows mark intervals of two standard deviations around those averages. [Colour figure can be viewed at wileyonlinelibrary.com].

Table 3 further presents reference heights defined in terms of the top-down scalar, namely the height of minimum mean gradient, $z_{{\rm i,g}\chi}$, and the height of maximum flux, $z_{{\rm i,f}\chi}$. After the initial transient, these reference heights become proportional to $z_{\rm enc}$ and independent of Re_0 (Figure 4). The corresponding heights defined in terms of the buoyancy satisfy $z_{{\rm i,g}b}/z_{\rm enc} = 1.24 \pm 0.01$ and $z_{{\rm i,f}b}/z_{\rm enc} = 1.15 \pm 0.01$ (Garcia and Mellado, 2014). Hence, the minimum scalar gradient occurs relatively close to the maximum buoyancy gradient, which will help later to derive entrainment-zone scales. In contrast, the scalar flux peaks at a distance $\approx 0.15\, z_{\rm enc}$ below the minimum buoyancy flux, which is more than half the entrainment-zone thickness (the entrainment-zone thickness is about $0.25\, z_{\rm enc}$). For typical midday atmospheric conditions $z_{\rm enc} \approx 1000$–2000 m; this result implies that the difference between the height of minimum buoyancy flux and maximum scalar flux is ≈ 150–300 m, which indicates that some entrainment-zone properties can differ significantly among scalar fields.

3.2. *Zero-order bulk model*

In this subsection, we derive a zero-order model for χ. Bulk models, such as the zero-order models sketched in Figure 1, provide simple but accurate representations of the bulk properties discussed in the previous subsection. Applied to the buoyancy, an integral analysis provides the following expressions for the properties defining the zero-order model (Fedorovich *et al.*, 2004, give a review):

$$h^{(0)} = \alpha^{(0)}\, z_{\rm enc}\,, \tag{22a}$$

$$b_{\rm ml}^{(0)} = \beta^{(0)}\, b_{\rm enc}\,, \tag{22b}$$

$$B_h^{(0)} = -A^{(0)}\, B_0\,. \tag{22c}$$

The variable $h^{(0)}$ is the CBL depth, $B_h^{(0)}$ is the buoyancy flux at the CBL top, and the superscript '0' indicates the zero-order model. Substituting Eqs (22) into the mixed-layer and the entrainment-rate equations for the buoyancy, we obtain that the model coefficients satisfy the following relationships:

$$A^{(0)} = \{(\alpha^{(0)})^2 - 1\}/2\,, \tag{23a}$$

$$\beta^{(0)} = (1 + A^{(0)})(1 + 2A^{(0)})^{-1}\alpha^{(0)}\,, \tag{23b}$$

having used the approximation $Re_0^{-1} \approx 0$. One of the three model coefficients $\{\alpha^{(0)}, \beta^{(0)}, A^{(0)}\}$ remains free. It is common practice to choose $h^{(0)}$ to coincide with the height of minimum buoyancy flux, $z_{{\rm i,f}b}$. For the equilibrium (quasi-steady) entrainment regime of a CBL growing into a linearly stratified atmosphere, we know that $\alpha^{(0)} = 1.15 \pm 0.01$ for this height (Garcia and Mellado, 2014), which implies $A^{(0)} = 0.16 \pm 0.01$ and $\beta^{(0)} = 1.01 \pm 0.01$. As a result, the model value $b_{\rm ml}^{(0)} \approx 1.01\, b_{\rm enc}$ agrees with the actual bulk value $b_{\rm ml} \approx 1.01\, b_{\rm enc}$.

For the top-down scalar, we can proceed similarly to the analysis of the buoyancy summarized above. The mixed-layer equation for χ is

$$h^{(0)}\frac{{\rm d}\chi_{\rm ml}^{(0)}}{{\rm d}t} = -w_{\rm e}^{(0)}(h^{(0)}/L_0 + \chi_{\rm ml}^{(0)}), \tag{24}$$

where

$$w_{\rm e}^{(0)} \equiv \frac{{\rm d}h^{(0)}}{{\rm d}t} = \alpha^{(0)} w_{\rm enc} \tag{25}$$

is the mean entrainment velocity associated with $h^{(0)}$. We assume that the CBL depth defined in terms of χ is the same as that defined in terms of b, i.e. $h^{(0)} = \alpha^{(0)} z_{\rm enc}$ is given from the bulk model for b. We could adopt a different CBL depth for χ, but this choice proves convenient for the description of q in section 4. Besides, the zero-order model is not designed to describe characteristics inside the entrainment zone (Fedorovich *et al.*, 2004), such as the differences between the flux-based reference heights of b and χ presented in the previous subsection. Then, Eq. (24) is an ordinary differential equation for the mixed-layer value as a function of time. We can express $\chi_{\rm ml}^{(0)}$ as a function of $h^{(0)}$ instead of t and write

$$h^{(0)} w_{\rm e}^{(0)}\frac{{\rm d}\chi_{\rm ml}^{(0)}}{{\rm d}h^{(0)}} = -w_{\rm e}^{(0)}(h^{(0)}/L_0 + \chi_{\rm ml}^{(0)}); \tag{26}$$

the initial condition is $\chi_{\rm ml}^{(0)} = 0$ at $h^{(0)} = 0$. The solution to this initial value problem is $-(1/2)h^{(0)}/L_0$, which can be written in terms of $\chi_{\rm enc}$ as (cf. Eq. (18))

$$\chi_{\rm ml}^{(0)} = \beta_\chi^{(0)}\, \chi_{\rm enc}\,, \qquad \beta_\chi^{(0)} = \alpha^{(0)}. \tag{27}$$

Using $\alpha^{(0)} \approx 1.15$ from the bulk model for the buoyancy, we obtain $\beta_\chi^{(0)} \approx 1.15$, which is very close to the value $\beta_\chi \approx 1.16$ obtained in the previous subsection (cf. Table 3). The mixed-layer value in the zero-order model approximates very well the actual mixed-layer value below $z \approx 0.8\, z_{\rm enc}$ (cf. Figure 3(a)).

The entrainment-rate equation provides the flux at the CBL top in the zero-order model:

$$F_{\chi,{\rm i}}^{(0)} = w_{\rm e}^{(0)}\left(\frac{h^{(0)}}{L_0} + \chi_{\rm ml}^{(0)}\right). \tag{28}$$

Substituting Eq. (25), Eq. (27) and $h^{(0)} = \alpha^{(0)} z_{\rm enc}$ into this equation, and using the approximation $z_{\rm enc} w_{\rm enc} \approx L_0^2 N$ (cf. Eq. (7)), we obtain

$$F_{\chi,{\rm i}}^{(0)} = (1/2 + A^{(0)})\, L_0 N\,. \tag{29}$$

Choosing $h^{(0)}$ equal to the height of minimum buoyancy flux, we obtain $1/2 + A^{(0)} \approx 0.66$. Figure 3(b) shows that the resulting model flux approximates very well the actual flux below $z \approx 0.8\, z_{\rm enc}$.

In summary, Eqs (27) and (29) accurately approximate bulk properties of the normalized top-down scalar. These equations

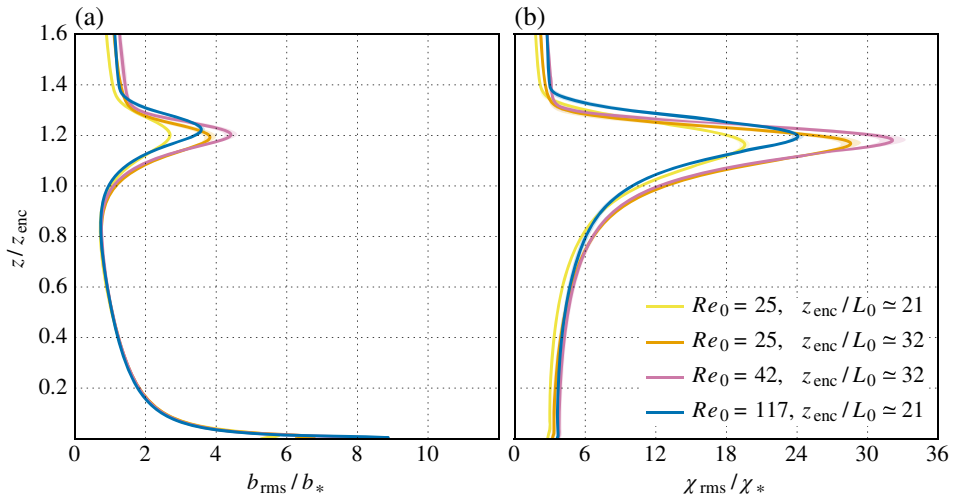

Figure 5. Normalized profiles of the rms of the turbulent fluctuation of (a) buoyancy and (b) top-down scalar. Lines indicate time averages over 3–8 convective time-scales z_{enc}/w_* (5–8% of z_{enc}/L_0), and shadows mark intervals of two standard deviations around those averages. [Colour figure can be viewed at wileyonlinelibrary.com].

Table 4. Self-similar constants of second- and third-order moments.

	Mixed layer					Entrainment zone			
Re_0	b_{rms}/b_*	χ_{rms}/χ_*	$\rho_{b\chi}$	S_b	S_χ	b_{rms}/b_δ	χ_{rms}/χ_δ	S_b	S_χ
25	1.06	4.23	0.17	1.89	−1.56	0.25	0.35	−2.60	7.85
42	1.06	4.50	0.17	1.84	−1.50	0.31	0.43	−2.75	8.70
117	1.04	4.35	0.14	1.80	−1.40	0.38	0.54	−3.15	9.25

Mixed-layer values are calculated at a height $z = 0.5\,z_{enc}$. Entrainment-zone values are maximum values. The buoyancy scale b_δ is defined as $N^2(0.1\,z_{enc} + \delta_b)$ (cf. Eq. (32)) and the scalar scale χ_δ is defined as $L_0^{-1}(0.31\,z_{enc} + \delta_\chi)$ (cf. Eq. (36)).

already provide a good characterization of the specific humidity in the pure drying regime. Additionally, we will use these results in section 4 to construct a bulk model for the specific humidity valid for arbitrary combinations of surface fluxes and lapse rates in the free atmosphere.

3.3. *Variance in the mixed layer*

The intensities of the turbulent fluctuations of the velocity and buoyancy in the mixed layer are characterized by the following convective scales (Deardorff, 1970):

$$w_* \equiv (B_0 z_{enc})^{1/3}, \tag{30a}$$

$$b_* \equiv B_0/w_*\,. \tag{30b}$$

This characterization means that temporally evolving vertical profiles of root-mean-square (rms) of the velocity components and buoyancy, when normalized with the CBL depth and w_* and b_*, become self-similar. Figure 5(a) illustrates this behaviour for the buoyancy, where $b_{rms} = \langle b'b'\rangle^{1/2}$. The dependence of the normalized rms on the state of development of the CBL, z_{enc}/L_0, and on the reference Reynolds number, Re_0, is less than 2% in the equilibrium (quasi-steady) entrainment regime (also Table 4).

Correspondingly, we conjecture that the convective scale

$$\chi_* \equiv (1/2)L_0 N/w_* \tag{31}$$

characterizes the intensity of the turbulent fluctuations of χ in the mixed layer. This expression is motivated by previous work using $\chi_* \approx F_{\chi,i}/w_*$ as convective scale (Moeng and Wyngaard, 1984; Moene *et al.*, 2006), and our previous finding that $L_0 N$ is a good estimate of the entrainment flux of the top-down scalar, $F_{\chi,i}$ (Figure 3(b)). The factor 1/2 is explained in section 4. Figure 5(b) supports this definition of convective scale, since the profiles of $\chi_{rms} = \langle \chi'\chi'\rangle^{1/2}$ below $z \approx 0.8\,z_{enc}$ become self-similar when normalized with the CBL depth and χ_* (also Table 4).

We observe in Figure 5 and Table 4 that the normalized rms of the top-down scalar in the mixed layer is significantly larger than that of the buoyancy. This behaviour has been well documented in the past, and it has often been attributed to the high production rates of χ^2_{rms} near the CBL top, where the magnitude of the mean scalar gradient is maximum (e.g. Deardorff, 1974; Moene *et al.*, 2006). However, our data indicate that this cannot be the only explanation, since we find a variance χ^2_{rms} near the CBL top that is larger than the variance $\{b_{rms}/(N^2 L_0)\}^2$ near the surface, but the latter has a higher production rate (not shown). High production rates of buoyancy variance near the surface are caused by the high mean gradient that develops near aerodynamically smooth surfaces (Mellado *et al.*, 2016) or near surfaces with a small roughness (e.g. Patton *et al.*, 2003). Hence, production rates of buoyancy variance near surfaces with small roughness can be larger than production rates of scalar variance in the entrainment zone, and still the scalar variance in the mixed layer can be larger. Thus, there must be other reasons for the larger variance of top-down scalars.

One reason we find is that the dissipation of variance of scalar fields is as important as its production in this comparison. The dissipation rate of buoyancy variance near the surface is large, whereas the dissipation rate of top-down scalar near the CBL top is small. This can be quantified in terms of the dissipation time scale, i.e. the ratio between the variance and its molecular dissipation rate (Moeng and Wyngaard, 1989). Figure 6 shows that the dissipation time-scale is about 3–6 times larger for the top-down scalar than for the buoyancy. We attribute this difference to

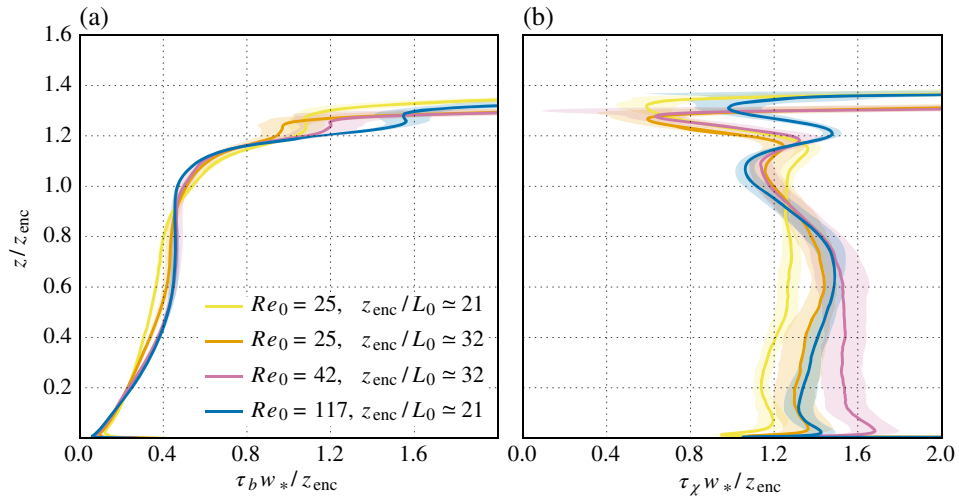

Figure 6. Normalized profiles of the dissipation time-scales of (a) buoyancy, $\tau_b = b_{rms}^2/\varepsilon_b$, and (b) top-down scalar, $\tau_\chi = \chi_{rms}^2/\varepsilon_\chi$. The dissipation rates are defined as $\varepsilon_b = 2\kappa\langle\partial_i b'\partial_i b'\rangle$ and $\varepsilon_\chi = 2\kappa\langle\partial_i\chi'\partial_i\chi'\rangle$. Lines indicate time averages over 3–8 convective time-scales z_{enc}/w_* (5–8% of z_{enc}/L_0), and shadows mark intervals of two standard deviations around those averages. [Colour figure can be viewed at wileyonlinelibrary.com].

the different length-scales at which variance is created: buoyancy variance near the surface is created at the surface scales, which are much smaller than the CBL depth (Mellado *et al.*, 2016), whereas top-down variance near the CBL top is generated at scales commensurate with the CBL depth. Hence, when surface scales are much smaller than the CBL depth, as depicted in Figure 2, the top-down variance needs more time to dissipate because it first needs to be transferred to the small scales through the break-up of large motions into smaller ones (the Richardson cascade process; Pope, 2000).

3.4. *Variance in the entrainment zone*

In the entrainment zone, convective scales do not characterize turbulent-fluctuation fields, since b_{rms}/b_* and χ_{rms}/χ_* are not self-similar there (Figure 5). Sorbjan (2005) proposed entrainment-zone scales based on the local mean gradients, which is supported by the significant correlation between the variance and the local mean gradient observed in simulations and measurements (e.g. Deardorff, 1974; Turner *et al.*, 2014). However, the dependence of the entrainment-zone mean gradients on the CBL depth and the meteorological conditions still needs to be provided. Garcia and Mellado (2014) derived first approximations for these dependencies for the case considered here, namely, a shear-free CBL penetrating into a linearly stratified atmosphere. Their analysis leads to the following scaling law for the maximum buoyancy rms:

$$b_{rms,i} \approx c_{b2}\, N^2 (0.1\, z_{enc} + \delta_b). \tag{32}$$

The length-scale

$$\delta_b \equiv -\frac{(b_{bg} - \langle b\rangle)_{z_{i,gb}}}{\{\partial_z (b_{bg} - \langle b\rangle)\}_{z_{i,gb}}} = \frac{N^2 z_{i,gb} - \langle b\rangle_{z_{i,gb}}}{(\partial_z \langle b\rangle)_{z_{i,gb}} - N^2} \tag{33}$$

is a gradient thickness characterizing the transition layer between the entrainment zone and the free atmosphere (cf. figure 5 in Garcia and Mellado, 2014). Henceforth, a subscript z_i next to a variable indicates that the variable is evaluated at that height, which in Eq. (33) is the height of maximum buoyancy gradient.

The derivation of Eq. (32) involves two assumptions. First, we assume

$$b_{rms,i} \propto \delta_b (\partial_z \langle b\rangle)_{z_{i,gb}} = N^2 \delta_b + (b_{bg} - \langle b\rangle)_{z_{i,gb}},$$

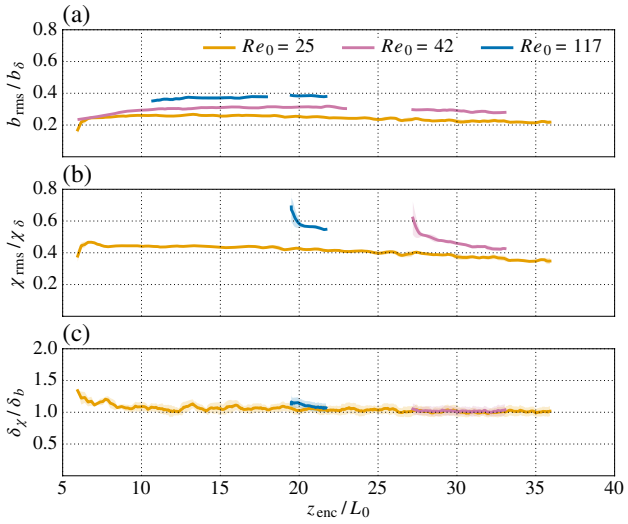

Figure 7. Temporal evolution of entrainment-zone properties: (a) buoyancy, (b) top-down scalar, and (c) gradient thickness. The buoyancy scale b_δ is defined as $N^2(0.1\, z_{enc} + \delta_b)$ (cf. Eq. (32)) and the scalar scale χ_δ is defined as $L_0^{-1}(0.31\, z_{enc} + \delta_\chi)$ (cf. Eq. (36)). Lines indicate time averages within an interval $\Delta z_{enc}/L_0 = 1$, and shadows mark intervals of two standard deviations around those averages. [Colour figure can be viewed at wileyonlinelibrary.com].

where the last equality follows from the definition of δ_b (Eq. (33)). Second, we assume that $\langle b\rangle_{z_{i,gb}}$ is a linear combination of $b_{ml} = \beta N^2 z_{enc}$ and $(b_{bg})_{z_{i,gb}} = N^2 z_{i,gb}$, where the first contribution represents the mean buoyancy at $z = z_{i,gb}$ inside the penetrating thermals and the second contribution represents the mean buoyancy outside them. The weighting factors of this linear combination would be the area fraction occupied by each region (Deardorff *et al.*, 1980). As a first approximation, we have considered an area fraction of 0.5, which explains the term $0.1\, z_{enc}$ in Eq. (32) because then

$$(b_{bg} - \langle b\rangle)_{z_{i,gb}} \approx N^2 (z_{i,gb} - \beta\, z_{enc})/2 \approx 0.1\, N^2 z_{enc},$$

having used the results $z_{i,gb} \approx 1.2\, z_{enc}$ and $\beta \approx 1.01$. (Garcia and Mellado, 2014, used $z_{i,gb} \approx 1.24\, z_{enc}$ and no area fraction, but in retrospect it seems physically reasonable to incorporate an area fraction in the derivation as explained above, even if the accuracy of Eq. (32) remains similar.) Figure 7(a) shows that this choice provides an approximation to $b_{rms,i}$ within 20%, which is the

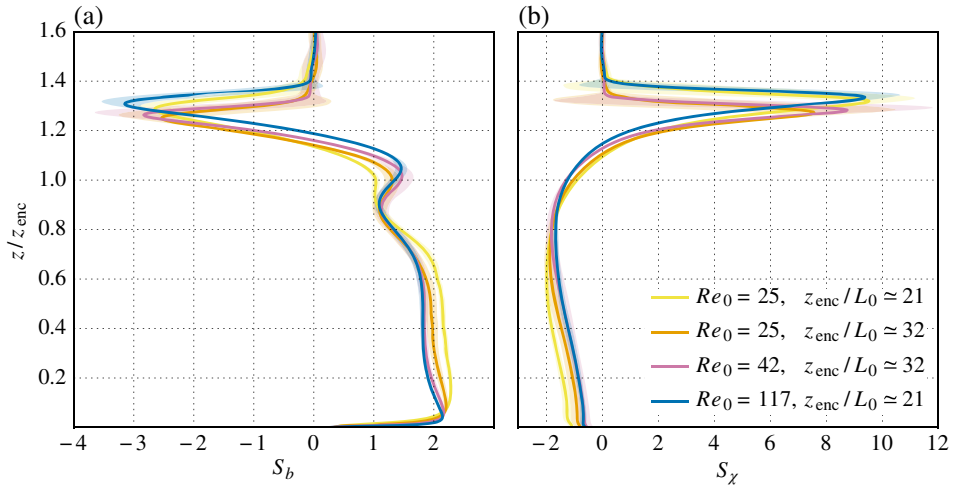

Figure 8. Profiles of the skewness of (a) buoyancy and (b) top-down scalar. Lines indicate time averages over 3–8 convective time-scales z_{enc}/w_* (5–8% of z_{enc}/L_0), and shadows mark intervals of two standard deviations around those averages. [Colour figure can be viewed at wileyonlinelibrary.com].

variation observed between the two cases with largest Reynolds numbers (also Table 4).

The gradient thickness can be approximated as (Garcia and Mellado, 2014)

$$\delta_b \approx 0.5\, w_*/N = 0.5\,(z_{enc}/L_0)^{1/3} L_0, \tag{34}$$

where the last equality follows from the definition of the convective velocity scale (Eq. (30a). According to this result and parcel theory, δ_b can be interpreted as a penetration depth of thermals into the free atmosphere: given a parcel of fluid with a vertical velocity proportional to w_* at its neutral-buoyancy level in a linearly stratified environment, the vertical displacement reached by that parcel of fluid is proportional to w_*/N, where N is the buoyancy frequency of the environment. Equation (34) shows that L_0 characterizes the upper region of the entrainment zone (Eq. (4)), since $0.5(z_{enc}/L_0)^{1/3} \approx 0.9$–$1.8$ for the range $z_{enc}/L_0 \approx 5$–50 that corresponds to typical midday atmospheric conditions.

Equations (32) and (34) show that, as the CBL grows, the contribution from $N^2 z_{enc}$ to $b_{rms,i}$ dominates, i.e. the buoyancy rms in the entrainment zone is increasingly determined by the encroachment scale $b_{enc} = N^2 z_{enc}$. However, for typical atmospheric values, δ_b can be a non-negligible fraction of the entrainment-zone thickness (e.g. 30% for $z_{enc}/L_0 \approx 20$) and the contribution from $N^2\delta_b$ is important.

Equations (32) and (34) also show that the intensity of the buoyancy fluctuation in the entrainment zone increases in time as the CBL grows. Physically, the reason is the increase in time of the difference between the buoyancy inside the penetrating thermals and outside them. In contrast, b_{rms} in the mixed layer decreases in time as the CBL grows, since b_* decreases according to Eqs (30); the mixed layer becomes better mixed.

For the top-down scalar, we can proceed similarly to the analysis of the buoyancy summarized above: first, we define a gradient thickness

$$\delta_\chi \equiv -\frac{(\chi_{bg} - \langle\chi\rangle)_{z_{i,g\chi}}}{\{\partial_z(\chi_{bg} - \langle\chi\rangle)\}_{z_{i,g\chi}}} = -\frac{L_0^{-1} z_{i,g\chi} + \langle\chi\rangle_{z_{i,g\chi}}}{(\partial_z\langle\chi\rangle)_{z_{i,g\chi}} + L_0^{-1}}; \tag{35}$$

then, we assume

$$\chi_{rms,i} \propto -\delta_\chi (\partial_z\langle\chi\rangle)_{z_{i,g\chi}} = L_0^{-1}\delta_\chi - (\chi_{bg} - \langle\chi\rangle)_{z_{i,g\chi}};$$

last, we estimate $\langle\chi\rangle_{z_{i,g\chi}}$ as the average between $\chi_{ml} = -(1/2)\beta_\chi L_0^{-1} z_{enc}$ and $(\chi_{bg})_{z_{i,g\chi}} = -L_0^{-1} z_{i,g\chi}$ (Eq. (10)). In this way, we obtain

$$\chi_{rms,i} \approx c_{\chi 2}\, L_0^{-1}(0.31\, z_{enc} + \delta_\chi), \tag{36}$$

having used the results $z_{i,g\chi} \approx 1.2\, z_{enc}$ and $\beta_\chi \approx 1.16$ (Table 3). In principle, δ_χ and δ_b could be different. However, Figure 7(c) shows that $\delta_\chi \approx \delta_b$, which implies that one single length-scale, namely the penetration depth, characterizes both scalars at the top of the entrainment zone. Hence, Eqs (34) and (36) provide the scalar rms in the entrainment zone as a function of the CBL depth and the meteorological conditions. The uncertainty in the approximation of $\chi_{rms,i}$ is also on the order of 20%, as inferred from Figure 7(b) and Table 4. Equation (36) indicates that, as occurred with the buoyancy, the scalar rms in the entrainment zone grows in time and it is increasingly determined by the encroachment scale.

3.5. *Skewness*

We conclude the discussion of the top-down scalar by analyzing its skewness, $S_\chi = \langle\chi'^3\rangle/\chi_{rms}^3$. In the entrainment zone, the skewness of the top-down scalar and the skewness of the buoyancy, $S_b = \langle b'^3\rangle/b_{rms}^3$, have opposite signs but otherwise a similar vertical structure (Figure 8). The skewness of the buoyancy is negative in the entrainment zone and reaches the absolute minimum at $z \approx 1.3\, z_{enc}$, i.e. above the height of maximum gradient (or maximum rms), which occurs at $z_{i,gb} \approx 1.2\, z_{enc}$. This negative skewness represents the penetration of updraughts into the free atmosphere: the tops of the updraughts occupy a small fraction of a horizontal cross-section and their buoyancy is smaller than that in the environment. Concomitantly, the skewness of the top-down scalar in the entrainment zone is positive, reaching an absolute maximum at $z \approx 1.3\, z_{enc}$, for a similar argument: moist updraughts are penetrating into an increasingly drier fluid. At $z/z_{enc} \approx 1.1$–1.2, i.e. slightly below the height of maximum magnitudes of the mean gradients (or maximum rms), the skewnesses reverse sign. This is caused by the entrainment of buoyant and dry air from the free atmosphere, which converges towards the centres of the subsiding regions. This behaviour agrees with previous observational and numerical data (Deardorff, 1974; Mahrt, 1991; Couvreux *et al.*, 2005; Turner *et al.*, 2014).

Further down into the mixed layer, differences in the vertical structure of S_b and S_χ become more prominent because of the

different boundary conditions at the surface. The top-down scalar has a zero surface flux, and mixed-layer properties are strongly determined by entrainment zone properties, the magnitude of the skewness decreasing from 2 at the top of the mixed layer to less than 1 near the surface. For the buoyancy, the surface flux induces a larger magnitude of the near-surface skewness, around 2, as a result of warm fluid particles converging towards the relatively narrow updraughts that define the cellular structure of the CBL.

We will see in the following section that the skewness of the specific humidity above $z \approx 0.8\, z_{\mathrm{enc}}$ is very similar to the skewness of the top-down scalar. However, below that height, the skewness of specific humidity can strongly vary with the meteorological conditions.

4. Specific humidity

Statistical properties of the specific humidity depend on $\{F_{q,0},\, \gamma_q,\, q_{\mathrm{bg},0}\}$ in addition to $\{z/z_{\mathrm{enc}},\, z_{\mathrm{enc}}/L_0\}$ and Re_0 (cf. section 2.2). However, dimensional analysis allows us to reduce the number of additional control parameters from three to essentially just one, which facilitates the analysis and description of moisture statistics. For that purpose, we write Eq. (11) in the non-dimensional form

$$(q - q_{\mathrm{bg},0})/q_{\mathrm{ref}} = \chi/\chi_{\mathrm{ref}} + \varphi\, b/b_{\mathrm{ref}}\,, \tag{37}$$

where

$$\varphi \equiv \frac{2N^2 F_{q,0}}{\gamma_q B_0 + N^2 F_{q,0}} = \frac{2F_{q,0}}{F_{q,\mathrm{ref}}} \tag{38}$$

is a flux-ratio parameter varying between 0 and 2. For notational convenience, we have introduced the following reference scales:

$$q_{\mathrm{ref}} \equiv (1/2)(L_0 N)^{-1} F_{q,\mathrm{ref}}\,, \tag{39a}$$

$$\chi_{\mathrm{ref}} \equiv (1/2)(L_0 N)^{-1} F_{\chi,\mathrm{ref}} = 1/2\,, \tag{39b}$$

$$b_{\mathrm{ref}} \equiv (1/2)(L_0 N)^{-1} F_{b,\mathrm{ref}} = N^2 L_0\,, \tag{39c}$$

where L_0 is defined in Eq. (4). The reference fluxes $F_{b,\mathrm{ref}} \equiv 2B_0$ and $F_{\chi,\mathrm{ref}} \equiv L_0 N$ are the sums of entrainment contributions $N^2 L_0 (L_0 N) = B_0$ and $L_0^{-1} L_0 (L_0 N) = L_0 N$, respectively, and surface contributions B_0 and 0. Analogously, we have defined

$$F_{q,\mathrm{ref}} \equiv F_{q,1} + F_{q,0}\,, \tag{40}$$

where

$$F_{q,1} \equiv \gamma_q B_0 N^{-2} = \gamma_q L_0 (L_0 N) \tag{41}$$

provides a reference scale for the entrainment flux of specific humidity in the drying regime, as demonstrated in the following sections. The last equality allows us to interpret $F_{q,1}$ as the product of a moisture scale $\gamma_q L_0$ and a velocity scale $L_0 N = (B_0 L_0)^{1/3}$. The prefactors 1/2 in the definitions of q_{ref}, b_{ref} and χ_{ref} result from the integral analysis of the corresponding evolution equations (as explained in section 3.1).

The choices of the flux-ratio parameter φ and the reference moisture flux $F_{q,\mathrm{ref}}$ to characterize the specific humidity are not unique and warrant further explanation. We could have chosen $F_{q,0}$ or $F_{q,1}$ instead of $F_{q,\mathrm{ref}}$, and we could have used $F_{q,1}/F_{q,0}$ instead of φ following previous studies of passive scalars in CBLs with an imposed strong inversion (e.g. Moeng and Wyngaard, 1984; de Roode *et al.*, 2004; Moene *et al.*, 2006). We favour φ, first because it naturally leads to the reference scales for moisture and moisture flux defined before (cf. Eqs (39a) and (40)) and the convective scale introduced in section 4.3 (cf. Eq. (61)), and these scales already account for a leading-order dependence of moisture statistics on meteorological conditions. At the same time, the condition $\varphi \approx 1$ still corresponds to $F_{q,1}/F_{q,0} \approx 1$, i.e. an entrainment flux comparable with the surface flux, which marks the transition between drying and moistening regimes (Mahrt, 1991).

A second reason for our choice of flux-ratio parameter and reference moisture flux is that they lead to weighting factors of order one in a bottom-up–top-down decomposition of the specific humidity field (cf. Eq. (37)):

$$(q - q_{\mathrm{bg},0})/q_{\mathrm{ref}} = \varphi\,(b/b_{\mathrm{ref}} + \chi) + (2 - \varphi)\,\chi\,. \tag{42}$$

The first term on the right-hand side is a bottom-up contribution proportional to φ; the normalized field $b/b_{\mathrm{ref}} + \chi$ has a zero lapse rate in the free atmosphere and a constant surface flux $L_0 N$. The second term is a top-down contribution proportional to $(2 - \varphi)$; the normalized field χ has a zero surface flux and a constant lapse rate that leads to an entrainment flux proportional to $L_0 N$ (cf. section 3.1).

In summary, the analysis of moisture statistics introduces solely one additional non-dimensional parameter, φ, and statistical properties of $(q - q_{\mathrm{bg},0})/q_{\mathrm{ref}}$ can be fully characterized as functions of two independent variables, $\{z/z_{\mathrm{enc}},\, z_{\mathrm{enc}}/L_0\}$, and two independent parameters, $\{\varphi,\, Re_0\}$. Typical mid-day atmospheric values are $B_0 \approx (0.3\text{–}1.0)\times 10^{-2}\,\mathrm{m^2\,s^{-3}}$, $N \approx (0.6\text{–}1.8)\times 10^{-2}\,\mathrm{s^{-1}}$, $\gamma_q \approx (0\text{–}2.0)\times 10^{-3}\,\mathrm{g\,kg^{-1}\,m^{-1}}$ and $F_{q,0} \approx (0.3\text{–}1.0)\times 10^{-1}\,\mathrm{g\,kg^{-1}\,m\,s^{-1}}$ (equivalently, latent heat fluxes $\approx (100\text{–}300)\,\mathrm{W\,m^{-2}}$, or evaporation rates $\approx (3\text{–}10)\,\mathrm{mm\,day^{-1}}$). Hence, we find $F_{q,1} \approx (0\text{–}5.0)\times 10^{-1}\,\mathrm{g\,kg^{-1}\,m\,s^{-1}}$, and φ can practically adopt any possible value between its theoretical limits, 0 and 2; we explore this interval in the following analysis.

For conciseness, we will discuss specific humidity properties derived only from the simulation with the highest Reynolds number, $Re_0 = 117$. The uncertainty in specific humidity properties due to Reynolds number effects is similar to that found in the properties of the buoyancy and the top-down scalar: of order 5% or less in mixed-layer properties, and of order 20% or less in entrainment-zone properties (cf. Table 4). Although 20% is arguably non-negligible, the observed Reynolds number dependence strongly indicates convergence towards Reynolds number similarity: a change of Reynolds number by a factor of 1.7 between $Re_0 = 25$ and $Re_0 = 42$ yields variations in entrainment-zone properties of $\approx 20\%$, which is the same variation observed when the Reynolds number is changed even more strongly, by a factor of ≈ 3, between $Re_0 = 42$ and $Re_0 = 117$. The Taylor-scale Reynolds number corresponding to $Re_0 = 117$ is

$$Re_\lambda \equiv u'\lambda/\nu = \sqrt{(20/3)Re_{\mathrm{t}}} \approx 160$$

(cf. Table 2), where $u' \equiv (2e/3)^{1/2}$ is the magnitude of the velocity fluctuation and $\lambda \equiv (15\nu u'^2/\varepsilon)^{1/2}$ is a Taylor length-scale (Pope, 2000). This convergence towards Reynolds number similarity at Taylor-scale Reynolds numbers $Re_\lambda \approx 100\text{–}200$ agrees with that reported in other turbulent flows (Dimotakis, 2000), and supports the conclusion reached in previous studies that DNS is becoming applicable to study atmospheric flows (e.g. Mellado, 2012; Jonker *et al.*, 2013; Waggy *et al.*, 2013; Garcia and Mellado, 2014; van Heerwaarden and Mellado, 2016).

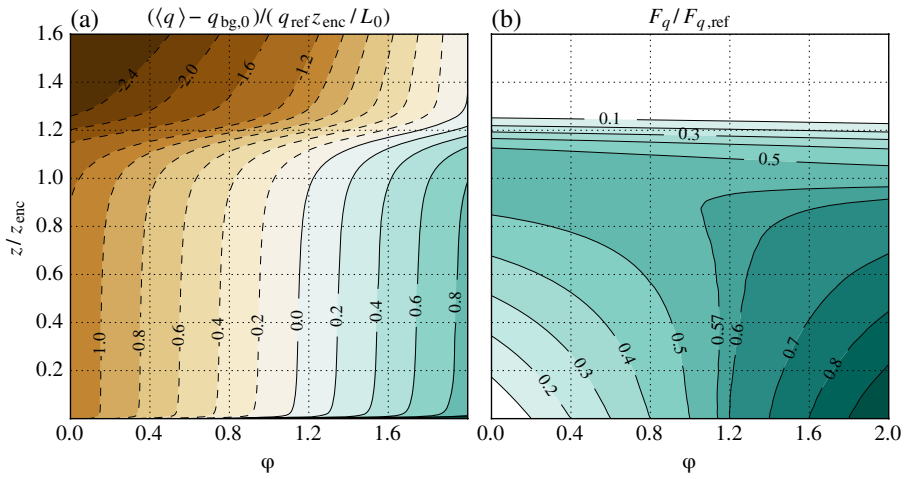

Figure 9. Contour plots of (a) the normalized mean specific humidity and (b) its mean vertical flux as a function of the normalized distance from the surface and the flux-ratio parameter φ (cf. Eq. (38)). $\varphi = 0$ corresponds to pure drying conditions and $\varphi = 2$ to pure moistening conditions. [Colour figure can be viewed at wileyonlinelibrary.com].

4.1. *Mean properties and bulk analysis*

Within this section, we will discuss statistical properties of the specific humidity in the same sequence as we discussed statistical properties of the top-down scalar in section 3. We start with the mean properties. Normalized mean properties of q can be obtained from

$$(\langle q\rangle - q_{bg,0})/(q_{ref} z_{enc}/L_0) = \langle\chi\rangle/(\chi_{ref} z_{enc}/L_0) + \varphi\,\langle b\rangle/(b_{ref} z_{enc}/L_0) \quad (43)$$

and

$$F_q/F_{q,ref} = F_\chi/F_{\chi,ref} + \varphi\, B/F_{b,ref}\,. \quad (44)$$

Equation (43) stems from Eq. (37), and Eq. (44) follows from Eq. (19) and the definitions of the mean vertical fluxes of buoyancy and specific humidity:

$$B \equiv \langle b'w'\rangle - \kappa\,\partial_z\langle b\rangle \quad (45)$$

and

$$F_q \equiv \langle q'w'\rangle - \kappa\,\partial_z\langle q\rangle\,. \quad (46)$$

In the equilibrium (quasi-steady) entrainment regime, the dependence of normalized mean properties on z_{enc}/L_0 is negligible (cf. section 3.1), and thus we only need to examine the dependence on $\{z/z_{enc}\,,\varphi\}$. This dependence is provided graphically in Figure 9. For $\varphi \approx 0$ we are close to the pure drying regime: the CBL dries because the flux of moisture out of the CBL (entrainment drying) dominates over the surface flux into the CBL (surface moistening). The flux increases from approximately 0 near the surface to a maximum near the inversion equal to

$$F_{q,i} \approx \{F_{\chi,i}/(L_0 N)\}\,F_{q,ref} \approx 0.56\,F_{q,1}\,, \quad (47)$$

as obtained by substituting $\varphi \approx 0$ into Eq. (44) and using the estimate $F_{\chi,i}/(L_0 N) \approx 0.56$ for the normalized entrainment flux of the top-down scalar (cf. Table 3). This maximum defines the entrainment flux of specific humidity in pure drying conditions. Hence, Eq. (47) confirms the interpretation of the parameter $F_{q,1}$ as a reference scale for the entrainment flux of specific humidity (cf. Eq. (41)). As φ increases – due to a slower growth of the CBL (smaller B_0 or larger N), due to a larger surface flux $F_{q,0}$, or due to a smaller lapse rate γ_q (cf. Eq. (38)) – the CBL dries less rapidly because surface moistening increasingly compensates entrainment drying. For values of φ slightly greater than 1, the surface moistening starts to dominate over entrainment drying (Figure 9(b)) and the CBL starts to moisten (Figure 9(a)). The cross-over value φ_{cr} that marks this transition between drying and moistening regimes will be obtained analytically below. For $\varphi \approx 2$ we approach the pure moistening regime: $F_{q,1}$ is negligible compare to $F_{q,0}$ and $F_{q,0}$ fully characterizes the mean vertical flux, which decreases from $F_{q,0}$ to $\approx F_{q,0}/2$ across the mixed layer (Figure 9(b)).

Analytically, we can obtain the vertically averaged specific humidity

$$q_{ml} \equiv z_{enc}^{-1}\int_0^{z_{enc}} \langle q\rangle\,\mathrm{d}z \quad (48)$$

by substituting $\langle q\rangle$ as provided by Eq. (43) into the right-hand side of the definition of q_{ml}, and using Eqs (13) and (14). This substitution yields

$$q_{ml} = q_{bg,0} + \beta_q\, q_{ref} z_{enc}/L_0\,, \quad (49)$$

where

$$\beta_q \equiv \varphi\,\beta - \beta_\chi\,. \quad (50)$$

The coefficients $\beta \approx 1.01$ and $\beta_\chi \approx 1.16$ characterize the mixed-layer values of buoyancy and top-down scalar (cf. section 3.1). The linear dependence of β_q on φ quantifies the linear variation with φ depicted in Figure 9(a). The condition $\beta_q = 0$ provides the cross-over value

$$\varphi_{cr} = \beta^{-1}\beta_\chi \approx 1.15 \quad (51)$$

to distinguish between the drying regime ($\varphi < \varphi_{cr}$) and the moistening regime ($\varphi > \varphi_{cr}$). The corresponding ratio between the surface flux and the reference flux is $(F_{q,0}/F_{q,ref})_{cr} = \varphi_{cr}/2 \approx 0.57$. Consistently, the contour in Figure 9(b) corresponding to this value is approximately vertical, indicating a constant vertical flux $F_q \approx F_{q,0}$ below $z \approx 0.8\,z_{enc}$. The ratio $F_{q,0}/F_{q,ref} \approx 0.57$ at $\varphi = \varphi_{cr}$ approximately coincides with the ratio $F_{q,i}/F_{q,ref} \approx 0.56$ at $\varphi = 0$ (cf. Eq. (47)). Hence, transition occurs when the surface flux of specific humidity, in units of $F_{q,ref}$, has increased

to match the entrainment flux of specific humidity in pure drying conditions. However, note that the entrainment flux concomitantly increases with $F_{q,0}$ because $F_{q,\mathrm{ref}}$ increases: at transition, the vertical flux of specific humidity below $z \approx 0.8\, z_{\mathrm{enc}}$ is $F_q \approx F_{q,0} = \varphi_{\mathrm{cr}}/(2-\varphi_{\mathrm{cr}})F_{q,1} \approx 1.35\, F_{q,1}$, which is more than twice the entrainment flux of specific humidity in the pure drying regime, $F_{q,\mathrm{i}} \approx 0.56\, F_{q,1}$.

The magnitude of q_{ml} is represented by $q_{\mathrm{ref}} z_{\mathrm{enc}}/L_0$. We can readily check that this scale provides the correct order of magnitude of mean specific humidity in the mixed layer. For typical atmospheric conditions, one finds $L_0 N \approx 1\,\mathrm{m\,s^{-1}}$ and $F_{q,\mathrm{ref}} = F_{q,0} + F_{q,1} \approx 0.1\text{–}0.6\,\mathrm{g\,kg^{-1}\,m\,s^{-1}}$, which implies $q_{\mathrm{ref}} = (1/2)F_{q,\mathrm{ref}}(L_0 N)^{-1} \approx 0.05\text{–}0.3\,\mathrm{g\,kg^{-1}}$; for a state of development of the CBL $z_{\mathrm{enc}}/L_0 \approx 10\text{–}50$, this implies mean specific humidities in the range $0.5\text{–}15\,\mathrm{g\,kg^{-1}}$, in agreement with observations (Couvreux *et al.*, 2005, 2007; Muppa *et al.*, 2016; Wulfmeyer *et al.*, 2016).

To conclude the bulk analysis of the specific humidity, we express q_{ml} in terms of the basic parameters by substituting Eqs (38) and (39a) into Eq. (49). This substitution yields

$$q_{\mathrm{ml}} = q_{\mathrm{bg},0} - 0.58\,\gamma_q z_{\mathrm{enc}} + 0.43\,(F_{q,0}/B_0)N^2 z_{\mathrm{enc}}\,, \tag{52}$$

where the numerical factors stem from $\beta_\chi/2 \approx 0.58$ and $\beta - \beta_\chi/2 \approx 0.43$. This expression shows explicitly the two contributions to q_{ml}: an entrainment contribution proportional to the lapse rate and a surface contribution proportional to the surface flux. This result further supports the definition of q_{ref} in Eq. (39a) because we can write this definition as $q_{\mathrm{ref}} = (1/2)\gamma_q L_0 + (1/2)(F_{q,0}/B_0)N^2 L_0$ and thus we can interpret q_{ref} as the sum of reference magnitudes of the entrainment and surface contributions in Eq. (52).

4.2. Zero-order bulk model

As discussed in section 3.2, a zero-order model provides a simple but accurate description of bulk properties, which motivates the construction of such a model for the specific humidity. A zero-order model for the specific humidity can be constructed by combining the zero-order models for the buoyancy and top-down scalar according to Eq. (37). For the mean specific humidity, this combination yields

$$q_{\mathrm{ml}}^{(0)} = q_{\mathrm{bg},0} + \beta_q^{(0)}\, q_{\mathrm{ref}} z_{\mathrm{enc}}/L_0\,. \tag{53}$$

The coefficient $\beta_q^{(0)}$ is defined by

$$\beta_q^{(0)} \equiv \varphi\, \beta^{(0)} - \beta_\chi^{(0)}, \tag{54}$$

where $\beta^{(0)}$ and $\beta_\chi^{(0)}$ are given in section 3.2 in terms of the model coefficient $\alpha^{(0)}$ (or, equivalently, $A^{(0)}$). The cross-over value of the flux-ratio parameter in the zero-order model is

$$\varphi_{\mathrm{cr}}^{(0)} = (\beta^{(0)})^{-1}\beta_\chi^{(0)} = \frac{2(\alpha^{(0)})^2}{1+(\alpha^{(0)})^2} \approx 1.14\,, \tag{55}$$

where the numerical value corresponds to $\alpha^{(0)} \approx 1.15$, i.e. the case in which the model CBL height is chosen to coincide with the height of minimum buoyancy flux.

For the flux of specific humidity, the combination of the zero-order models for the buoyancy and top-down scalar leads to a linear profile that varies between $F_{q,0}$ at the surface and

$$F_{q,\mathrm{i}}^{(0)} = (1/2)\left\{1 + (2-\varphi)A^{(0)}\right\} F_{q,\mathrm{ref}} \tag{56}$$

at the CBL top. Substituting $\varphi = \varphi_{\mathrm{cr}}^{(0)}$ into this expression yields $(F_{q,\mathrm{i}}^{(0)})_{\mathrm{cr}} = F_{q,0}$, which implies a constant vertical flux in the mixed layer and thus a steady mean specific humidity at transition between drying and moistening regimes, as expected.

In terms of the basic parameters (cf. Figure 1), the zero-order model can be summarized as

$$q_{\mathrm{ml}}^{(0)} = q_{\mathrm{bg},0} - 0.58\gamma_q z_{\mathrm{enc}} + 0.43(F_{q,0}/B_0)N^2 z_{\mathrm{enc}}\,, \tag{57a}$$

$$F_{q,\mathrm{i}}^{(0)} = 0.5\, F_{q,0} + 0.66\, \gamma_q B_0 N^{-2}, \tag{57b}$$

where the numerical factors stem from $\beta_\chi^{(0)}/2 \approx 0.58$, $\beta^{(0)} - \beta_\chi^{(0)}/2 \approx 0.43$ and $1/2 + A^{(0)} \approx 0.66$. The good approximation to the parametric dependence of q_{ml} in Eq. (52) by the parametric dependence of $q_{\mathrm{ml}}^{(0)}$ in Eq. (57a) stems from the good approximation of b_{ml} and χ_{ml} by $b_{\mathrm{ml}}^{(0)}$ and $\chi_{\mathrm{ml}}^{(0)}$, respectively (cf. section 3.2). Equations (57) provide the leading-order dependence of mean properties of specific humidity on the surface fluxes and lapse rates in the free atmosphere. This is the first result that we were looking for.

4.3. Variance in the mixed layer

As mentioned in the introduction, not only mean properties but also properties of the turbulent fluctuations of specific humidity are key for understanding cloud formation. We discuss the variance and the skewness of the specific humidity during the remaining sections, focusing on the dependence of these statistical properties on the surface fluxes and lapse rates in the free atmosphere.

The turbulent fluctuation of the specific humidity, $q' \equiv q - \langle q \rangle$, can be expressed as a linear combination of the turbulent fluctuations of b and χ by subtracting Eq. (43) multiplied by z_{enc}/L_0 from Eq. (37):

$$q'/q_{\mathrm{ref}} = \chi'/\chi_{\mathrm{ref}} + \varphi\, b'/b_{\mathrm{ref}}\,. \tag{58}$$

Hence, the specific humidity variance can be obtained from

$$q_{\mathrm{rms}}^2/q_{\mathrm{ref}}^2 = (\chi_{\mathrm{rms}}/\chi_{\mathrm{ref}})^2 + \varphi^2(b_{\mathrm{rms}}/b_{\mathrm{ref}})^2 + 2\varphi\rho_{b\chi}(\chi_{\mathrm{rms}}/\chi_{\mathrm{ref}})(b_{\mathrm{rms}}/b_{\mathrm{ref}}). \tag{59}$$

In addition to the profiles b_{rms} and χ_{rms}, discussed in section 3.3, we need the correlation coefficient $\rho_{b\chi} \equiv \langle b'\chi' \rangle/(b_{\mathrm{rms}}\chi_{\mathrm{rms}})$ as a function of $\{z/z_{\mathrm{enc}},\, z_{\mathrm{enc}}/L_0\}$ to obtain the specific humidity variance as a function of $\{z/z_{\mathrm{enc}},\, z_{\mathrm{enc}}/L_0,\, \varphi\}$. This correlation coefficient is presented in Figure 10(a). We see that the dependence of $\rho_{b\chi}$ on the state of development of the CBL, z_{enc}/L_0, is small, less than 5% of the variation with the normalized height, z/z_{enc}, so that we can consider $\rho_{b\chi}$ to be solely a function of the normalized height as a first approximation. The vertical variation of $\rho_{b\chi}$ with height is similar to the vertical variation of the correlation between temperature and specific humidity reported previously in the literature (Deardorff, 1974; Mahrt, 1991): it is positive in the lower part of the CBL because of warm and moist thermals, and negative in the upper part because of entrainment of warm and dry air. Here we find a similar structure even in the absence of surface moistening (the surface flux of χ is zero), which indicates that the warm thermals are still less dry than the fluid between them because of mixing along the recirculation paths followed by the entrained air.

When looking for scaling laws for q_{rms}, we have to consider the mixed layer and the entrainment zone separately. In the mixed layer, the convective scales defined by Eqs (30) and (31) are the

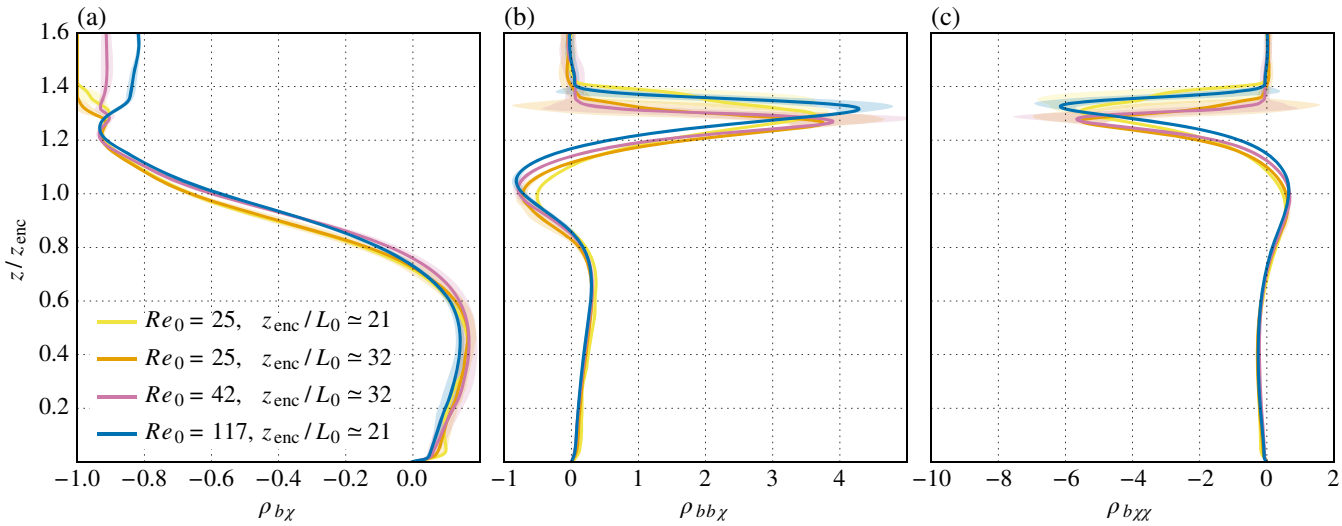

Figure 10. Profiles of (a) correlation coefficient and (b, c) normalized third-order moments of buoyancy and top-down scalar. Lines indicate time averages over 3–8 convective time-scales z_{enc}/w_* (5–8% of z_{enc}/L_0), and shadows mark intervals of two standard deviations around those averages. [Colour figure can be viewed at wileyonlinelibrary.com].

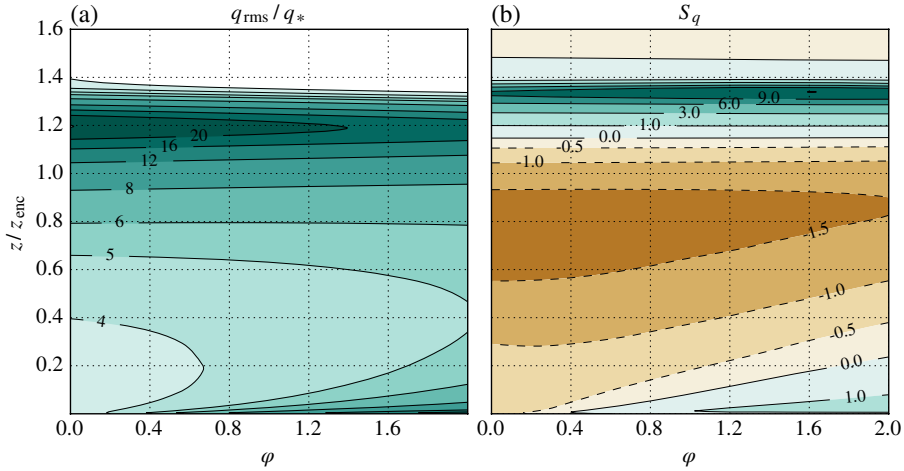

Figure 11. Contour plots of the normalized specific humidity (a) rms and (b) skewness as a function of the normalized distance from the surface and the flux-ratio parameter φ (cf. Eq. (38)): $\varphi = 0$ corresponds to pure drying conditions and $\varphi = 2$ to pure moistening conditions. [Colour figure can be viewed at wileyonlinelibrary.com].

appropriate scales. We can rewrite Eq. (59) as

$$q_{rms}^2/q_*^2 = (\chi_{rms}/\chi_*)^2 + \varphi^2(b_{rms}/b_*)^2 + 2\varphi\,\rho_{b\chi}(\chi_{rms}/\chi_*)(b_{rms}/b_*), \tag{60}$$

having defined

$$q_* \equiv (1/2)F_{q,ref}/w_* \tag{61}$$

as convective scale of the specific humidity, and having used the relationships $q_*/q_{ref} = b_*/b_{ref} = \chi_*/\chi_{ref} = L_0N/w_*$. This expression for the convective scale stems from

$$q_*w_* = \int_0^1 \{F_{q,0}z/h + F_{q,1}(1 - z/h)\}\,\mathrm{d}(z/h)\,, \tag{62}$$

i.e. q_*w_* is equated to the vertical average of a linear reference flux that varies from $F_{q,0}$ at the surface to $F_{q,1}$ at the CBL top (e.g. Cuijpers and Holtslag, 1998; Moene *et al.*, 2006). This definition of convective scale generalizes Deardorff's definition (Deardorff, 1970), which retains only a surface-flux contribution.

The function $q_*^{-1}q_{rms}(z/z_{enc}, \varphi)$ is provided graphically in Figure 11(a). We observe that this function is relatively constant in the centre of the mixed layer. Analytically, we can use the coefficients in Table 4 to write

$$q_{rms} = 4.3(1 + 0.068\,\varphi + 0.057\,\varphi^2)^{1/2}\,q_*\,, \tag{63}$$

valid for $z = 0.5\,z_{enc}$. This expression shows that q_{rms}/q_* in the centre of the mixed layer varies less than 20% with φ, which supports q_* as characteristic scale for the specific humidity rms. Therefore, the dependence of q_{rms} on the meteorological conditions is well characterized by the dependence of q_*. In terms of the basic parameters, the convective scale is

$$q_* = (1/2)F_{q,0}/w_* + (1/2)F_{q,1}/w_*\,. \tag{64}$$

Hence, the variance increases whenever the surface flux or entrainment flux of specific humidity increases because the humidity difference between the ascending and descending branches of the convective cells increases. Concomitantly, as the CBL grows or the surface flux B_0 strengthens, w_* increases and the variance decreases because the air is better mixed. For typical atmospheric conditions, one finds $F_{q,ref} = F_{q,0} + F_{q,1} \approx 0.1\text{–}0.6\,\mathrm{g\,kg^{-1}\,m\,s^{-1}}$ and $w_* \approx 2\,\mathrm{m\,s^{-1}}$, which implies $q_* \approx 0.02\text{–}0.15\,\mathrm{g\,kg^{-1}}$. Hence, the specific humidity rms is on the order of $0.1\text{–}0.7\,\mathrm{g\,kg^{-1}}$ in the mixed layer, which is consistent with measurements (Wulfmeyer, 1999; Couvreux *et al.*, 2007; Muppa *et al.*, 2016; Wulfmeyer *et al.*, 2016).

However, near the surface and in the entrainment zone, the ratio $q_{\rm rms}/q_*$ varies more strongly with φ than in the mixed layer, confirming that the convective scale q_* is not appropriate in those regions (Figure 11(a)). The variance increases with the surface flux faster than q_* near the surface ($q_{\rm rms}/q_*$ grows with φ), and slower than q_* in the entrainment zone ($q_{\rm rms}/q_*$ diminishes with φ). The reason for this behaviour is that the increasingly stronger surface flux causes increasingly stronger near-surface fluctuations, but this enhancement weakens away from the surface due to mixing.

Last, we note that, in the pure moistening regime ($\varphi \approx 2$), the near-surface variance becomes comparable to the entrainment-zone variance (Figure 11(a)). This occurs despite production rates near the surface being more than ten times as large (not shown). The reason for this apparent contradiction was already exposed in section 3.3: near the surface, the variance concentrates in the small scales and dissipation rates are large enough to compensate the higher production rates. Hence, the large humidity variance in the entrainment zone is not only due to large production rates, but also due to small dissipation rates.

4.4. Variance in the entrainment zone

In the upper part of the entrainment zone, where the variance of buoyancy and top-down scalar peak, b and χ are strongly anti-correlated (cf. Figure 10(a)). Vertical motions in a region where the mean gradients of buoyancy and scalar have opposite sign cause positive buoyancy fluctuations that coincide with negative scalar fluctuations. Using the approximation $\rho_{b\chi,{\rm i}} \approx -1.0$ in Eq. (59), together with Eqs (32) and (36), we obtain

$$q_{\rm rms,i} \approx q_{\rm ref} L_0^{-1} \{0.23\, z_{\rm enc} + (1.08 - 0.38\,\varphi)(0.1\, z_{\rm enc} + \delta_b)\} \qquad (65)$$

as an estimate for the specific humidity rms in the entrainment zone, having used the results $c_{b2} \approx 0.38$ and $c_{\chi 2} \approx 0.54$ (cf. Table 4). Equation (65) has a form similar to Eqs (32) and (36) for the buoyancy and the top-down scalar, respectively, and it can be interpreted similarly, namely as a scaling law $q_{\rm rms,i} \propto -\delta_q (\partial_z \langle q\rangle)_{z_{{\rm i},gq}} = \gamma_q \delta_q - (q_{\rm bg} - \langle q\rangle)_{z_{{\rm i},gq}}$, where δ_q is a gradient thickness defined similarly to δ_b in Eq. (33) or δ_χ in Eq. (35) (Appendix B). The magnitude of $q_{\rm rms,i}$ is represented by $\approx 0.3\, q_{\rm ref} z_{\rm enc}/L_0$, i.e. 30% of the typical mixed-layer value (cf. Eq. (49)). Therefore, Eq. (65) predicts that the specific humidity rms in the entrainment zone is on the order of 0.3–4.5 g kg^{-1}, which is consistent with measurements (Wulfmeyer, 1999; Couvreux *et al.*, 2005, 2007; Turner *et al.*, 2014; Muppa *et al.*, 2016; Wulfmeyer *et al.*, 2016).

Equation (65), along with Eq. (63), is the second main result that we were looking for, since both expressions allow us to calculate the rms in the mixed layer and in the entrainment zone for arbitrary combinations of surface fluxes and lapse rates in the free atmosphere (cf. Figure 1).

4.5. Skewness

Using Eq. (58), the third-order moment of the specific humidity can be obtained from the third-order moments of the buoyancy and top-down scalar according to

$$\frac{\langle q'^3\rangle}{q_*^3} = S_\chi \left(\frac{\chi_{\rm rms}}{\chi_*}\right)^3 + \varphi^3\, S_b \left(\frac{b_{\rm rms}}{b_*}\right)^3 + 3\varphi \left(\frac{\chi_{\rm rms}}{\chi_*}\right)\left(\frac{b_{\rm rms}}{b_*}\right)\left\{\rho_{b\chi\chi}\left(\frac{\chi_{\rm rms}}{\chi_*}\right) + \varphi \rho_{bb\chi}\left(\frac{b_{\rm rms}}{b_*}\right)\right\}. \qquad (66)$$

We have expressed $\langle q'^3\rangle/q_*^3$ in terms of the skewness of the buoyancy and the top-down scalar, S_b and S_χ, and in terms of $\rho_{bb\chi} \equiv \langle b'^2\chi'\rangle/(b_{\rm rms}^2 \chi_{\rm rms})$ and $\rho_{b\chi\chi} \equiv \langle b'\chi'^2\rangle/(b_{\rm rms}\chi_{\rm rms}^2)$. The reason is that, in the mixed layer, these normalized terms are approximately independent of the state of development of the CBL, $z_{\rm enc}/L_0$ (Figures 8 and 10(b) and (c)), so that the leading-order dependence of $\langle q'^3\rangle$ on $z_{\rm enc}/L_0$ is captured by $b_{\rm rms}$, $\chi_{\rm rms}$ and the convective scales. In the entrainment zone, the region of strong vertical variation in those profiles slightly descends and narrows as the CBL grows, which is due to the slight decrease over time of the entrainment-zone thickness relative to $z_{\rm enc}$ (Garcia and Mellado, 2014). However, the change in magnitude with $z_{\rm enc}/L_0$ remains small, within statistical convergence. The dependence on the Reynolds number also remains small, within statistical convergence. Hence, we focus on the dependence on $z/z_{\rm enc}$ and φ.

From Eqs (60) and (66), we can obtain the skewness $S_q \equiv \langle q'^3\rangle/q_{\rm rms}^3$. The function $S_q(z/z_{\rm enc}, \varphi)$ is provided graphically in Figure 11(b). For $\varphi \approx 0$, i.e. in the pure entrainment-drying regime, we recover the skewness of the top-down scalar (cf. Figure 8(b)). The predominance of negative skewness in the mixed layer for the drying regime has been well documented in the past, and it is associated with tongues of dry air from the free atmosphere penetrating deep into the CBL (Deardorff, 1974; Mahrt 1991; Couvreux *et al.*, 2005; Lanotte and Mazzitelli, 2013). These tongues are clearly visible in Figure 2.

As we increase the flux-ratio parameter, the skewness remains practically invariant above $z \approx 0.8\, z_{\rm enc}$, i.e. the skewness in the upper part of the CBL is practically the same in the drying and moistening regimes. The skewness is on the order of -1 in the upper part of the mixed-layer, becomes positive slightly below the height of minimum mean gradient or maximum rms ($z_{{\rm i},gq} \approx 1.2\, z_{\rm enc}$), and reaches a maximum above it, at $z \approx 1.3\, z_{\rm enc}$. This behaviour is consistent with previous data from observations and simulations (Deardorff, 1974; Couvreux *et al.*, 2007; Turner *et al.*, 2014; Muppa *et al.*, 2016).

In contrast, S_q varies strongly with φ below $z \approx 0.8\, z_{\rm enc}$, and in the lower 20% of the CBL S_q can even change from negative in the drying regime to positive in the moistening regime. The use of the sign of the skewness to distinguish between drying and moistening regimes has often been discussed in the literature. Mahrt (1991) proposes such an approach based on the analysis of the source term in the evolution equation of $\langle q'^3\rangle$ for the limiting cases of pure drying or pure moistening. However, Couvreux *et al.* (2007) shows that the transport term is also important, and the correspondence between the sign of the skewness and the type of regime should be restricted at most to the lower part of the CBL. Here, we further see that this is also not the case because the relationship between the sign of the skewness and the type of regime depends not only on φ but also on the distance to the surface (cf. Figure 11(b)): between $z \approx 0.1\, z_{\rm enc}$ and $z \approx 0.2\, z_{\rm enc}$, we can have a negative skewness in half of the moistening regime ($\varphi \gtrsim \varphi_{\rm cr} \approx 1.15$); below $z \approx 0.1\, z_{\rm enc}$, we can have a positive skewness in half of the drying regime ($\varphi \lesssim \varphi_{\rm cr} \approx 1.15$). Hence, knowing sign of the skewness is often insufficient to distinguish between drying and moistening regimes.

5. Conclusions

We have developed parametrizations for the first three moments and the mean vertical flux of specific humidity in the equilibrium (quasi-steady) entrainment regime of cloud-free CBLs without

a mean wind. The analysis has been based on a top-down–bottom-up decomposition. Appropriately combining the buoyancy and top-down scalar, we have constructed the specific humidity field for arbitrary combinations of control parameters $\{B_0, N^2, \gamma_q, F_{q,0}\}$, where B_0 and $-N^2$ are the surface flux and lapse rate of buoyancy, and $F_{q,0}$ and γ_q are the surface flux and lapse rate of specific humidity.

Direct numerical simulations have been used to ascertain the coefficients of the scaling laws. The sensitivity of the results to the Reynolds number is $\approx 5\%$ or less in mixed-layer properties, and $\approx$20% or less in entrainment-zone properties, despite changes in Reynolds number by a factor of 3. This degree of Reynolds number similarity further supports the applicability of direct numerical simulations to investigate some aspects of atmospheric turbulence.

We have first studied mean properties and the transition between drying and moistening regimes. We have shown that the entrainment flux of specific humidity in the pure drying regime is commensurate with $\gamma_q B_0 N^{-2}$. Based on this result, we have demonstrated that the flux-ratio parameter $\varphi = 2F_{q,0}/(F_{q,0} + \gamma_q B_0 N^{-2})$ proves convenient to characterize the statistical properties of the specific humidity: it varies between 0 for the pure drying regime and 2 for the pure moistening regime, and the transition between drying and moistening regimes occurs at $\varphi_{\rm cr} \approx 1.15$. This condition corresponds to $F_{q,0} \approx 1.35\,\gamma_q B_0 N^{-2}$, a relationship that allows us predict the moisture regime of the shear-free CBL for given meteorological conditions. Based on these results, we have constructed a zero-order model for the specific humidity (Eqs (57)).

We have then discussed the rms of q. We have demonstrated that, in the mixed layer, the convective scale $q_* = (1/2)(F_{q,0} + \gamma_q B_0 N^{-2})/w_*$ explains more than 80% of the variation of the specific humidity rms with φ. A parametrization for the remaining 20% variation has also been provided, in case it is needed (Eq. (63)). As expected, the convective scale does not characterize the near-surface region nor the entrainment zone. Near the surface, the specific humidity rms increases faster with φ than the convective scale, and in the entrainment zone slower. The reason is that the increase of the surface flux with φ enhances near-surface fluctuations, but this enhancement weakens away from the surface due to mixing. The specific humidity rms in the entrainment zone has been parametrized based on entrainment-zone scales (Eq. (65)). We have also demonstrated that the large rms in the entrainment zone is not only due to large production rates, but also due to low dissipation rates.

Last, we have studied the skewness. The skewness of q is negative in the mixed layer and becomes positive slightly below the height of minimum mean gradient of q (or maximum rms), in agreement with previous observational and numerical data. In addition, we have found that this behaviour is independent of φ, i.e. independent of the surface fluxes and lapse rates in the free atmosphere. However, in the lower 20% of the CBL depth, the skewness depends strongly on both the vertical distance from the surface and the meteorological conditions. Between $z \approx 0.1\,z_{\rm enc}$ and $z \approx 0.2\,z_{\rm enc}$, the skewness is negative in half of the moistening regime ($\varphi \gtrsim \varphi_{\rm cr} \approx 1.15$); below that region, the skewness is positive in half of the drying regime ($\varphi \lesssim \varphi_{\rm cr} \approx 1.15$). Hence, using a positive skewness near the surface as an indicator of the moistening regime, as conjectured before based on single-case studies, is not robust.

Appendices

Appendix A: Proof of Eq. (11)

Let use construct the following scalar field:

$$\xi = q - q_{\rm bg,0} - (F_{q,0}/B_0)\, b - \left\{\gamma_q L_0 + (F_{q,0}/B_0) N^2 L_0\right\} \chi \,. \tag{A1}$$

From the evolution equations for q, b and χ, we obtain that the evolution equation for ξ is

$$\partial_t \xi + u_j \partial_j \xi = \kappa\, \partial_{jj} \xi, \tag{A2}$$

with the Neumann boundary conditions $\partial_z \xi = 0$ at the top and bottom boundaries, and the background profile is $\xi_{\rm bg} = 0$. Hence, ξ tends to zero as turbulence mixes vertically any initial condition of ξ. The solution $\xi = 0$ implies Eq. (11), which is what we wanted to demonstrate.

Provided an initial condition $\xi \neq 0$ within a depth δ_ξ next to the surface, an estimate for the rate of decrease of ξ once $z_{\rm enc} \gtrsim \delta_\xi$ can be obtained from the evolution of the vertically averaged value

$$\frac{1}{z_{\rm enc}} \int_0^{z_\infty} \langle \xi \rangle \, {\rm d}z.$$

Since the vertical integral of $\langle \xi \rangle$ is constant, the vertically averaged value decreases as $z_{\rm enc}^{-1}$, i.e. as $t^{-1/2}$ (Eq. (7)).

Appendix B: Interpretation of Eq. (65)

Here we demonstrate that Eq. (65) for $q_{\rm rms,i}$ can be interpreted similarly to Eq. (32) for $b_{\rm rms,i}$ and Eq. (36) for $\chi_{\rm rms,i}$, namely as an approximation to the rms in the entrainment zone by the product of the gradient thickness and the local mean gradient,

$$q_{\rm rms,i} \approx -c_{q2}\, \delta_q (\partial_z \langle q \rangle)_{z_{{\rm i},gq}} \,. \tag{B1}$$

$z_{{\rm i},gq}$ is the height of minimum gradient of the mean specific humidity, and the gradient thickness of the specific humidity is defined by

$$\delta_q \equiv -\frac{(q_{\rm bg} - \langle q \rangle)_{z_{{\rm i},gq}}}{\{\partial_z (q_{\rm bg} - \langle q \rangle)\}_{z_{{\rm i},gq}}}. \tag{B2}$$

We organize the discussion in two steps. As a first step, we relate $z_{{\rm i},gq}$ and δ_q to the corresponding properties of the buoyancy and top-down scalar using Eq. (43). This equation and the approximation $z_{{\rm i},g\chi} \approx z_{{\rm i},gb}$, which is satisfied within 5% (cf. section 3), imply that the minimum mean gradient of q also occurs near that height, i.e. $z_{{\rm i},gq} \approx z_{{\rm i},gb}$. We denote that common height by $z_{\rm i,g}$. With this result, we can substitute Eq. (43) into Eq. (B2) and use Eqs (33) and (35) to obtain

$$(\delta_q - \delta_\chi) \chi_{\rm ref}^{-1} \{\partial_z (\chi_{\rm bg} - \langle \chi \rangle)\}_{z_{\rm i,g}} + \varphi\, (\delta_q - \delta_b) b_{\rm ref}^{-1} \{\partial_z (b_{\rm bg} - \langle b \rangle)\}_{z_{\rm i,g}} = 0 \,. \tag{B3}$$

Since $\delta_\chi \approx \delta_b$ (cf. Figure 7(c)) and this equation needs to be satisfied for any φ, the solution is $\delta_q \approx \delta_b$. We denote that common thickness by δ.

As a second step, we recall that the definitions of δ yield

$$\begin{aligned} \delta (\partial_z \langle b \rangle)_{z_{\rm i,g}} &= N^2 \delta + (b_{\rm bg} - \langle b \rangle)_{z_{\rm i,g}}, \\ -\delta (\partial_z \langle \chi \rangle)_{z_{\rm i,g}} &= L_0^{-1} \delta - (\chi_{\rm bg} - \langle \chi \rangle)_{z_{\rm i,g}}, \\ -\delta (\partial_z \langle q \rangle)_{z_{\rm i,g}} &= \gamma_q \delta - (q_{\rm bg} - \langle q \rangle)_{z_{\rm i,g}}. \end{aligned} \tag{B4}$$

The mean values in the right-hand side are unknown. As a first approximation, we estimate them as an average between the values inside and outside the penetrating thermals,

$$\begin{aligned}\langle b\rangle_{z_{\mathrm{i,g}}} &= \sigma\, b_{\mathrm{ml}} + (1-\sigma)(b_{\mathrm{bg}})_{z_{\mathrm{i,g}}},\\ \langle \chi\rangle_{z_{\mathrm{i,g}}} &= \sigma\, \chi_{\mathrm{ml}} + (1-\sigma)(\chi_{\mathrm{bg}})_{z_{\mathrm{i,g}}},\\ \langle q\rangle_{z_{\mathrm{i,g}}} &= \sigma\, q_{\mathrm{ml}} + (1-\sigma)(q_{\mathrm{bg}})_{z_{\mathrm{i,g}}},\end{aligned} \tag{B5}$$

where $0 \leq \sigma \leq 1$ is an intermittency factor, i.e. the area fraction occupied by the penetrating thermals in a horizontal cross-section at $z = z_{\mathrm{i,g}}$. We obtain the following expressions:

$$\begin{aligned}\delta(\partial_z\langle b\rangle)_{z_{\mathrm{i,g}}} &= N^2\delta + \sigma\,\{(b_{\mathrm{bg}})_{z_{\mathrm{i,g}}} - b_{\mathrm{ml}}\},\\ -\delta(\partial_z\langle \chi\rangle)_{z_{\mathrm{i,g}}} &= L_0^{-1}\delta - \sigma\,\{(\chi_{\mathrm{bg}})_{z_{\mathrm{i,g}}} - \chi_{\mathrm{ml}}\},\\ -\delta(\partial_z\langle q\rangle)_{z_{\mathrm{i,g}}} &= \gamma_q\delta - \sigma\,\{(q_{\mathrm{bg}})_{z_{\mathrm{i,g}}} - q_{\mathrm{ml}}\},\end{aligned} \tag{B6}$$

Substituting into these equations the result $z_{\mathrm{i,g}} \approx 1.2\, z_{\mathrm{enc}}$ (cf. Table 3) and the parametrizations for the mixed-layer values derived in sections 3.1 and 4.1, we obtain

$$\begin{aligned}\delta(\partial_z\langle b\rangle)_{z_{\mathrm{i,g}}} &= b_{\mathrm{ref}}L_0^{-1}\{\delta + \sigma\,(1.2-\beta)z_{\mathrm{enc}}\},\\ -\delta(\partial_z\langle \chi\rangle)_{z_{\mathrm{i,g}}} &= \chi_{\mathrm{ref}}L_0^{-1}\{2\delta + \sigma(2.4-\beta_\chi)z_{\mathrm{enc}}\},\\ -\delta(\partial_z\langle q\rangle)_{z_{\mathrm{i,g}}} &= q_{\mathrm{ref}}L_0^{-1}\{(2-\varphi)\delta + \sigma\,[1.2(2-\varphi)+\beta_q]z_{\mathrm{enc}}\}.\end{aligned} \tag{B7}$$

Using $\sigma = 1/2$, the first equation multiplied by c_{b2} yields Eq. (32), and the second equation multiplied by $c_{\chi 2}$ yields Eq. (36). We now show that the third equation multiplied by c_{q2} approximates Eq. (65). For that purpose, we note that the previous expressions satisfy

$$\frac{-\delta(\partial_z\langle q\rangle)_{z_{\mathrm{i,g}}}}{q_{\mathrm{ref}}} = \frac{-\delta(\partial_z\langle \chi\rangle)_{z_{\mathrm{i,g}}}}{\chi_{\mathrm{ref}}} - \varphi\frac{\delta(\partial_z\langle b\rangle)_{z_{\mathrm{i,g}}}}{b_{\mathrm{ref}}}, \tag{B8}$$

which implies

$$\frac{q_{\mathrm{rms,i}}}{c_{q2}q_{\mathrm{ref}}} = \frac{\chi_{\mathrm{rms,i}}}{c_{\chi 2}\chi_{\mathrm{ref}}} - \varphi\frac{b_{\mathrm{rms,i}}}{c_{b2}b_{\mathrm{ref}}}. \tag{B9}$$

If we approximate the constants $c_{b2} \approx 0.38$ and $c_{\chi 2} \approx 0.54$ (cf. Table 4) by their mean value 0.46, which is valid within 20%, and we assume $c_{q2} \approx 0.46$, we can write

$$\frac{q_{\mathrm{rms,i}}}{q_{\mathrm{ref}}} \approx \frac{\chi_{\mathrm{rms,i}}}{\chi_{\mathrm{ref}}} - \varphi\frac{b_{\mathrm{rms,i}}}{b_{\mathrm{ref}}}. \tag{B10}$$

This equation leads to Eq. (65), which is what we wanted to demonstrate.

Acknowledgements

We thank Axel Seifert, Dmitrii Mironov and Dave Turner for motivating and instructive discussions on the topic. Data for case $Re_0 = 25$ was provided by Armin Haghshenas. The authors gratefully acknowledge the Gauss Centre for Supercomputing (GCS) for providing computing time through the John von Neumann Institute for Computing (NIC) on the GCS share of the supercomputer JUQUEEN at Jülich Supercomputing Centre (JSC). Funding was provided by the Max Planck Society through its Max Planck Research Groups program. Primary data and scripts used in the analysis and other supporting information which may be useful in reproducing the authors' work are archived by the Max Planck Institute for Meteorology and can be obtained by contacting publications@mpimet.mpg.de.

References

Carpenter MH, Kennedy CA. 1994. 'Fourth-order 2N-storage Runge–Kutta schemes', Technical report TM-109112. NASA Langley Research Center: Hampton, VA.

Carson DJ, Smith FB. 1975. Thermodynamic model for the development of a convectively unstable boundary layer. *Adv. Geophys.* **18A**: 111–124.

Coleman GN, Ferziger JH, Spalart PR. 1990. A numerical study of the turbulent Ekman layer. *J. Fluid Mech.* **213**: 313–348.

Couvreux F, Guichard F, Redelsperger JL, Kiemle C, Masson V, Lafore JP, Flamant C. 2005. Water vapour variability within a convective boundary-layer assessed by large-eddy simulations and IHOP_2002 observations. *Q. J. R. Meteorol. Soc.* **131**: 2665–2693.

Couvreux F, Guichard F, Masson V, Redelsperger JL. 2007. Negative water vapour skewness and dry tongues in the convective boundary layer: Observation and large-eddy simulation budget anaylsis. *Boundary-Layer Meteorol.* **123**: 269–294.

Cuijpers JWM, Holtslag AAM. 1998. Impact of skewness and non-local effects on scalar and buoyancy fluxes in convective boundary layers. *J. Atmos. Sci.* **55**: 151–162.

Deardorff JW. 1970. Convective velocity and temperature scales for the unstable planetary boundary layer and for Rayleigh convection. *J. Atmos. Sci.* **27**: 1211–1213.

Deardorff JW. 1974. Three-dimensional numerical study of turbulence in an entraining mixed layer. *Boundary-Layer Meteorol.* **7**: 199–226.

Deardorff JW, Willis GE, Stockton BH. 1980. Laboratory studies of the entrainment zone of a convectively mixed layer. *J. Fluid Mech.* **100**: 41–64.

de Roode SR, Duynkerke PG, Jonker HJJ. 2004. Large-eddy simulation: How large is large enough? *J. Atmos. Sci.* **61**: 403–421.

Dimotakis PE. 2000. The mixing transition in turbulent flows. *J. Fluid Mech.* **409**: 69–98.

Fedorovich E, Conzemius R, Mironov D. 2004. Convective entrainment into a shear-free linearly stratified atmosphere: Bulk models reevaluated through large-eddy simulation. *J. Atmos. Sci.* **61**: 281–295.

Frigo M, Johnson SG. 2005. The design and implementation of FFTW3. *Proceedings of the IEEE*, Ulaby FT. (ed): **93**: 216–231. Institute of Electrical and Electronics Engineers, Inc.: New York, USA. https://doi.org/10.1109/JPROC.2004.840301.

Garcia JR, Mellado JP. 2014. The two-layer structure of the entrainment zone in the convective boundary layer. *J. Atmos. Sci.* **71**: 1935–1955.

Jonker HJJ, van Reeuwijk M, Sullivan PP, Patton EG. 2013. On the scaling of shear driven entrainment: A DNS study. *J. Fluid Mech.* **732**: 150–165.

Lanotte A, Mazzitelli I. 2013. Scalar turbulence in convective boundary layers by changing the entrainment flux. *J. Atmos. Sci.* **70**: 248–265.

Lele SK. 1992. Compact finite difference schemes with spectral-like resolution. *J. Comput. Phys.* **103**: 16–42.

Lewellen WS, Yoh S. 1993. Binormal model of ensemble partial cloudiness. *J. Atmos. Sci.* **50**: 1228–1237.

Lilly DK. 1968. Models of cloud-topped mixed layers under strong inversion. *Q. J. R. Meteorol. Soc.* **94**: 292–309.

Mahrt L. 1991. Boundary-layer moisture regimes. *Boundary-Layer Meteorol.* **152**: 151–176.

Mellado JP. 2012. Direct numerical simulation of free convection over a heated plate. *J. Fluid Mech.* **712**: 418–450.

Mellado JP, Ansorge C. 2012. Factorization of the Fourier transform of the pressure-Poisson equation using finite differences in colocated grids. *Z. Angew. Math. Mech.* **92**: 380–392.

Mellado JP, van Heerwaarden CC, Garcia JR. 2016. Near-surface effects of free atmosphere stratification in free convection. *Boundary-Layer Meteorol.* **159**: 69–95.

Moene AF, Michels BI, Holtslag AAM. 2006. Scaling variances of scalars in a convective boundary lazer under different entrainment regimes. *Boundary-Layer Meteorol.* **120**: 257–274.

Moeng C-H, Wyngaard JC. 1984. Statistics of conservative scalars in the convective boundary layer. *J. Atmos. Sci.* **41**: 3161–3169.

Moeng C-H, Wyngaard JC. 1989. Evaluation of turbulent transport and dissipation closures in second-order modelling. *J. Atmos. Sci.* **46**: 2311–2330.

Moin P, Mahesh K. 1998. Direct numerical simulation: A tool in turbulence research. *Annu. Rev. Fluid Mech.* **30**: 539–578.

Muppa SK, Behrendt A, Späth F, Wulfmeyer V, Metzendorf S, Riede A. 2016. Turbulence humidity fluctuations in the convective boundary layer: Case studies water vapour differential absorption lidar measurements. *Boundary-Layer Meteorol.* **158**: 43–66.

Naumann AK, Seifert A, Mellado JP. 2013. A refined statistical cloud closure using double-Gaussian probability density functions. *Geosci. Model Dev.* **6**: 1641–1657.

Neggers R, Stevens B, Neelin JD. 2006. A simple equilibrium model for shallow-cumulus-topped mixed layers. *Theor. Comput. Fluid Dyn.* **20**: 305–322.

Ozmidov RV. 1965. On the turbulent exchange in a stably stratified ocean. *Izv. Atmos. Oceanic Phys. Ser.* **1**: 853–860.

Panton RL. 2005. *Incompressible Flow* (3rd edn). Wiley: New York, NY.

Patton EG, Sullivan PP, Davis KJ. 2003. The influence of a forest canopy on top-down and bottom-up diffusion in the planetary boundary layer. *Q. J. R. Meteorol. Soc.* **129**: 1415–1434.

Pope SB. 2000. *Turbulent Flows*. Cambridge University Press: Cambridge, UK.

Siebert H, Shaw RA. 2017. Supersaturation fluctuations during the early stage of cumulus formation. *J. Atmos. Sci.* **74**: 975–988.

Smyth WD, Moum JN. 2000. Length scales of turbulence in stably stratified mixing layers. *Phys. Fluids* **12**: 1327–1342.

Sorbjan Z. 2005. Statistics of scalar fields in the atmospheric boundary layer based on large-eddy simulations. Part 1: Free convection. *Boundary-Layer Meteorol.* **116**: 467–486.

Sullivan PP, Moeng CH, Stevens B, Lenschow DH, Mayor SD. 1998. Structure of the entrainment zone capping the convective atmospheric boundary layer. *J. Atmos. Sci.* **55**: 3042–3064.

Turner D, Wulfmeyer V, Berg LK, Schween JH. 2014. Water vapor turbulence profiles in stationary continental convective boundary layers. *J. Geophys. Res. Atmos.* **119**: 11151–11165. https://doi.org/10.1002/2014JD022202.

van Heerwaarden CC, Mellado JP. 2016. Growth and decay of a convective boundary layer over a surface with a constant temperature. *J. Atmos. Sci.* **73**: 2165–2177.

Waggy SB, Biringen S, Sullivan PP. 2013. Direct numerical simulation of top-down and bottom-up diffusion in the convective boundary layer. *J. Fluid Mech.* **724**: 581–606.

Wulfmeyer V. 1999. Investigations of humidity skewness and variance profiles in the convective boundary layer and comparison of the latter with large-eddy simulation results. *J. Atmos. Sci.* **56**: 1077–1087.

Wulfmeyer V, Muppa SK, Behrendt A, Hammann E, Späth F, Sorbjan Z, Turner D, Hardesty RM. 2016. Determination of convective boundary layer entrainment fluxes, dissipation rates, and the molecular destruction of variances: Theoretical description and a strategy for its confirmation with a novel Lidar system synergy. *J. Atmos. Sci.* **73**: 667–692.

Wyngaard JC. 2010. *Turbulence in the Atmosphere*. Cambridge University Press: Cambridge, UK.

Wyngaard JC, Brost R. 1984. Top-down and bottom-up diffusion of a scalar in a convective boundary layer. *J. Atmos. Sci.* **41**: 102–112.